

**Key Points:**

- We generate synthetic images of the energetic neutral atom (ENA) flux from the magnetosphere-atmosphere interactions at Europa and Callisto
- Detectable ENA emissions form a segmented ring around each moon's disc; the ring's angular and radial structure is governed by ion gyroradii
- When Europa and Callisto are near the center of Jupiter's plasma sheet, the magnetic draping pattern is visible from certain vantage points

**Correspondence to:**

C. M. Haynes,  
mhaynes@eas.gatech.edu

**Citation:**

Haynes, C. M., Tippens, T., Simon, S., & Liuzzo, L. (2025). Constraints on the observability of energetic neutral atoms from the magnetosphere-atmosphere interactions at Callisto and Europa. *Journal of Geophysical Research: Space Physics*, 130, e2024JA033391. <https://doi.org/10.1029/2024JA033391>

Received 30 SEP 2024

Accepted 17 DEC 2024

## Constraints on the Observability of Energetic Neutral Atoms From the Magnetosphere-Atmosphere Interactions at Callisto and Europa

C. Michael Haynes<sup>1</sup> , Tyler Tippens<sup>1</sup>, Sven Simon<sup>1,2</sup> , and Lucas Liuzzo<sup>3</sup> 

<sup>1</sup>School of Earth and Atmospheric Sciences, Georgia Institute of Technology, Atlanta, GA, USA, <sup>2</sup>School of Physics, Georgia Institute of Technology, Atlanta, GA, USA, <sup>3</sup>Space Sciences Laboratory, University of California, Berkeley, Berkeley, CA, USA

**Abstract** We investigate the emission of energetic neutral atoms (ENAs) from the magnetosphere-atmosphere interactions at Europa and Callisto that may be observed by an ENA imaging instrument. To do so, we combine the draped electromagnetic fields from the AIKEF hybrid model with a tracing tool for the energetic magnetospheric parent ions. Using a realistic viewing geometry, synthetic ENA images are generated for multiple detector positions and orientations with respect to the magnetospheric field. At both moons, we investigate the ENA emission morphology at different distances to the center of Jupiter's plasma sheet. By generating ENA images for uniform electromagnetic fields as a baseline, we also constrain the influence of field line draping and induction signals on the observable ENA emission signatures. Our major findings are: (a) In uniform fields, regions of elevated ENA flux in the images populate segments of a ring around each moon's disc. (b) The radial and angular extensions of these segments decrease with growing magnetospheric field strength. (c) The angle between the detector's boresight vector and the ambient field determines the regions of the images populated with elevated ENA flux. (d) Non-uniformities in the fields are discernible in the ENA images only when Europa and Callisto are located near the center of Jupiter's plasma sheet. Even in this case, the visibility of such features is restricted to certain viewing geometries. (e) Anisotropies in the moons' atmospheric density profiles produce gradients in the observable ENA emissions. This facilitates a global characterization of these neutral envelopes through ENA imaging.

### 1. Introduction

Europa (radius  $R_E = 1560.8$  km) and Callisto (radius  $R_C = 2410.3$  km) are both moons of Jupiter that maintain nearly circular, tidally locked orbits in the planet's equatorial plane, located at radial distances of  $9.4R_J$  and  $26.3R_J$ , respectively (Jupiter's radius:  $R_J = 71,492$  km). The surfaces of these moons are rich in water ice, and each has a tenuous atmosphere generated in part through sublimation (e.g., Galli et al., 2018; Spencer et al., 1999) and sputtering (e.g., Addison et al., 2022; Carberry Mogan et al., 2023; Vorburger & Wurz, 2018). Europa's neutral envelope consists largely of molecular oxygen (Hall et al., 1995, 1998; Roth et al., 2016) with a secondary contribution from water vapor. Specifically, observations from the Hubble Space Telescope revealed the existence of a localized increase in  $H_2O$  density, peaking around Europa's subsolar (or ramside) apex with a column density comparable to that of  $O_2$  near this point (Roth, 2021). Other water group products have been detected in Europa's atmosphere at concentrations below 5% (e.g., Roth et al., 2016, 2017). At Callisto,  $CO_2$  was the first atmospheric constituent identified by using UV observations taken by the Galileo spacecraft during the C10 flyby (Carlson, 1999; Carlson et al., 1996). However, molecular oxygen was subsequently found to be the dominant component, with its number density near the surface exceeding that of  $CO_2$  by over an order of magnitude (Cunningham et al., 2015; Kliore et al., 2002). Europa's and Callisto's atmospheres are partially ionized by electron impacts and solar UV photons (e.g., Carberry Mogan et al., 2022; Gurnett et al., 2000; Saur et al., 1998), generating ionospheres around these moons.

The orbits of Callisto and Europa are embedded within Jupiter's magnetosphere, and as such, the moons are constantly exposed to the planet's magnetic field. Along Europa's orbit, Jupiter's internal field provides the dominant contribution to the magnetospheric field (Connerney et al., 2018, 2022). As distance from the planet's magnetic axis increases –that is, moving from Europa's to Callisto's orbit– a growing contribution stems from the equatorial current sheet (Connerney et al., 2020; Khurana, 1997). Jupiter's magnetic moment is misaligned by about  $9.6^\circ$  with respect to its spin axis; consequentially, the distance of Europa and Callisto to the magnetic equator

periodically varies. At this equator, the magnetic field is oriented approximately southward. Above and below the magnetic equator, the field is still (to within about  $30^\circ$ ) southward at Europa's orbit, but the contribution of the current sheet causes a largely radial field orientation near Callisto (e.g., Connerney et al., 2018; Liuzzo et al., 2022). The Jovian magnetic moment, as perceived at the positions of Europa or Callisto, can be decomposed into a constant component aligned with Jupiter's rotation axis and a time-varying (horizontal) component in the moons' orbital plane. Over a synodic period of Jupiter (10.18 hr at Callisto and 11.23 hr at Europa) each moon experiences one complete rotation of this horizontal component (Khurana et al., 2009; Kivelson et al., 2000; Zimmer et al., 2000). This periodicity in the ambient magnetic field induces a secondary field in any conducting layers at Europa and Callisto (Seufert et al., 2011), such as a salty subsurface ocean (Vance et al., 2018, 2021; Zimmer et al., 2000) or a conductive ionosphere (Hartkorn & Saur, 2017). These induction signals can perturb the Jovian magnetospheric field near Europa's or Callisto's surfaces by upwards of 20% and 60%, respectively (e.g., Khurana et al., 1998; Kivelson et al., 2000; Seufert et al., 2011; Vance et al., 2018).

Jupiter's magnetosphere contains a thermal plasma population with energies  $E \lesssim 1$  keV, transporting synchronously with the magnetic field and confined to a disc-like sheet concentrated about the centrifugal equator (Bagenal & Delamere, 2011; Phipps & Bagenal, 2021). Moving away from the center of the plasma sheet in the north-south direction, the density of the thermal plasma decreases rapidly. Therefore, over a synodic rotation, the ambient plasma density at Europa and Callisto changes periodically. Due to Jupiter's fast rotation, the thermal plasma constantly impinges upon Europa's and Callisto's trailing hemispheres at a relative velocity of about 100 – 200 km/s (Bagenal et al., 2015, 2016; Kivelson et al., 2004). At both moons, newly created ionospheric ions are picked up by the magnetospheric fields and carried downstream, mass-loading the incident plasma flow. The deflection of the thermal plasma by the moons' ionospheres and induced fields causes the magnetospheric field to pile up around their trailing (ramside) hemispheres, forming a draping pattern. At large distances, this pattern connects to a system of Alfvén wings that ultimately reach Jupiter's polar ionosphere (Neubauer, 1980, 1998, 1999) and can excite auroral footprints (e.g., Bhattacharyya et al., 2018; Bonfond et al., 2017; Moirano et al., 2024). The field enhancement in Callisto's pile-up region may exceed five times the ambient magnetospheric field strength (Liuzzo et al., 2022), whereas it remains below 50% of the background field at Europa (Kivelson et al., 1999, 2009). Due to the periodic variation in the upstream plasma conditions and magnetic field at these moons, the strength and shape of the perturbations vary with the Jovian synodic frequency, too (Addison et al., 2021; Harris et al., 2021; Schilling et al., 2007).

### 1.1. Emission of Energetic Neutral Atoms

In addition to the thermal plasma, a population of energetic magnetospheric ions and electrons with energies  $E > 1$  keV exists throughout Jupiter's magnetosphere (e.g., Clark et al., 2019; Mauk et al., 2004; Paranicas et al., 2000). These particles bounce along magnetospheric field lines while drifting azimuthally. When interacting with Europa or Callisto, energetic ions and electrons can be described as a test particle population subject to the magnetospheric fields (e.g., Addison et al., 2021, 2022, 2023; Liuzzo et al., 2019a, 2019b, 2024; Nordheim et al., 2022). The energetic ion population is comprised of mostly protons, oxygen, and sulfur (e.g., Clark et al., 2020; Cohen et al., 2001; Paranicas et al., 2000) which constantly bombard the atmospheres and surfaces of Europa and Callisto. When Callisto is near the center of Jupiter's magnetospheric plasma sheet, energetic sulfur and oxygen ions heavily irradiate the region around the ramside apex, with their influx reduced by about a factor of two at other locations on the moon's surface (Liuzzo et al., 2019b, 2022). The energetic protons bombard Callisto nearly uniformly, apart from a 50% drop in influx around the Jupiter-averted apex. Moving from the center to far outside the Jovian plasma sheet, the influx of all three ion species maximizes near the Jupiter-averted and Jupiter-facing apices (Liuzzo et al., 2022). For the case of Europa located at the center of Jupiter's plasma sheet, the energetic ion influx is minimized around the ramside apex for all three species (Addison et al., 2021). This localized reduction in surface irradiation is still present when Europa is far from the center of the sheet; in this case, an additional depletion in the precipitation pattern stretches around the moon along its equator. Comparing energetic ion precipitation obtained for uniform and draped fields, the influx at both Europa and Callisto is reduced by a factor of 2–5 at most surface locations when the field perturbations are taken into account. Even so, the draped fields allow energetic ions to irradiate regions on the surface which are inaccessible in uniform fields, and vice versa (Addison et al., 2021; Breer et al., 2019; Liuzzo et al., 2019b, 2022).

Not all of the incident energetic ions impact Europa's and Callisto's surfaces and contribute to their erosion (Addison et al., 2021; Carberry Mogan et al., 2023; Haynes et al., 2023). Some interact with the moons'

atmospheres through charge exchange, where the energetic ion strips an electron from a neutral particle. At Europa, such charge exchange processes were found to contribute to the reductions in energetic proton fluxes observed during Galileo's flybys of the moon (Huybrighs et al., 2023). Charge exchange between energetic ions and atmospheric neutrals is highly forward-scattered, so the newly created Energetic Neutral Atom (ENA) travels away with the momentary velocity of the parent ion at the moment of charge exchange (e.g., Dandouras & Amsif, 1999; Lindsay & Stebbings, 2005). The kinetic energy of an ENA is vast compared to its potential energy in the gravitational fields of the Jovian system, so it propagates along a straight line (e.g., Mauk, Allegrini, et al., 2020; Mauk, Clark, et al., 2020; Mauk et al., 2003). As revealed by the model of Haynes et al. (2023), ENAs generated through charge exchange with Callisto's and Europa's atmospheres typically have energies between 5 – 100 keV. This is because the energetic ion abundance is reduced below a few keV (Mauk et al., 2004; Paranicas et al., 2002), and the cross sections for charge exchange decline steeply above energies of 100 keV (Lindsay & Stebbings, 2005).

Plasma and magnetometer observations of moon-magnetosphere interactions are taken only along the one-dimensional trajectory of the spacecraft. Thus, multiple flybys with distinct trajectories under nearly identical upstream conditions are required to (approximately) reconstruct the three-dimensional structure of the plasma interaction region. ENA imaging instruments such as the Ion and Neutral CAmera (INCA; Krimigis et al., 2004; Mitchell et al., 1996) aboard the Cassini spacecraft use the incoming flux of ENAs to construct a two-dimensional image during a certain flyby, loosely analogous to the operation of a CCD camera for visible light. The perturbed electromagnetic fields guide the trajectories of the energetic ions, some of which are converted into ENAs moving along tangent lines of the parent ion trajectories within the atmosphere. Since the trajectories of the energetic ions within the moon's interaction region determine the ENA emission pattern, ENA imaging can partially overcome the limitations of in situ plasma and magnetic field data by providing global "snapshots" of the draped fields (e.g., Kabanovic et al., 2018; Tippens et al., 2022; Wulms et al., 2010).

ENA images from INCA have served as a valuable diagnostic tool in characterizing the interaction between Titan and Saturn's magnetospheric plasma, which produces qualitatively similar electromagnetic structures as Callisto's and Europa's magnetospheric interactions (e.g., Brandt et al., 2012; Liuzzo et al., 2015; Mitchell et al., 2005). Along Cassini's path to the Saturnian system, ENA images were captured as the spacecraft passed the Jovian magnetosphere, but only Jupiter's atmosphere and the Europa neutral torus were resolved at the spacecraft's large distance from the planet (Mauk et al., 2003; Smith et al., 2019). To date, a spacecraft with an ENA detector has not yet imaged the moon-magnetosphere interactions at Europa or Callisto, but the JUpiter ICy moons Explorer (JUICE) is, at the time of this writing, en route to become the first (Grasset et al., 2013; Tosi et al., 2024). It carries the JENI instrument, capable of detecting ENAs between energies of 0.5–300 keV (Galli et al., 2022). Thus, ENA images taken by JUICE will provide a unique opportunity to understand the properties of Europa's and Callisto's plasma interaction regions on a global scale, complementing in situ plasma and magnetometer observations.

## 1.2. Modeling ENA Emissions From Moon-Plasma Interactions

To provide context for the upcoming JUICE observations at Europa and Callisto, Haynes et al. (2023) combined the three-dimensional electromagnetic field output from the AIKEF hybrid model (thermal kinetic ions, fluid electrons; Müller et al., 2011) with a tracing model for the energetic parent ions to calculate the ENA flux from charge exchange with these moons' atmospheres. ENA detectors aboard spacecraft have a limited angular field of view (FOV) and are point-like on the length scales of the plasma interaction (e.g., Krimigis et al., 2004). Therefore, only a tiny fraction of the emitted ENA population is sampled by an actual spacecraft instrument, and a large set of observations from different vantage points is needed to capture the global emission morphology. To obtain a global picture of the emitted ENA population, Haynes et al. (2023) generated maps of the ENA flux through a hypothetical, concentric spherical detector around each moon's neutral envelope. These maps reveal the locations on the detector sphere hit by ENAs, independent of their velocity vectors at impact. Such a spherical ENA detector records the *entire* ENA population leaving the moons' atmospheres, that is, it captures the global morphology of atmospheric ENA emissions detectable from outside the neutral envelope. To assess the variability of ENA emissions at Europa and Callisto over a synodic rotation, Haynes et al. (2023) considered two locations of each moon with respect to Jupiter's magnetospheric plasma sheet: at the center and at maximum distance below the center. By comparing the modeled maps of ENA flux through their spherical detector in draped fields to those generated for uniform fields, the authors isolated which features of the ENA emissions are caused by field perturbations from plasma interaction currents.

At Europa and Callisto, Haynes et al. (2023) found that the majority of detectable ENA emissions are focused into a band of high ENA flux centered around the great circle on the detector sphere that is perpendicular to the ambient magnetospheric field. With changing distance between each moon and the center of the Jovian plasma sheet, this band is rotated on the detector sphere according to the change in orientation of the ambient magnetospheric field vector. The fraction of observable ENA flux confined to the band is controlled by the ratio of the energetic ion gyroradii to the moon's atmospheric scale height: the more gyrations a parent ion can carry out within the atmosphere, the greater the likelihood of it undergoing charge exchange and emitting an ENA into the band. In the strong magnetospheric field at Europa, parent ions with pitch angles near 90° traverse a path through the atmosphere 10–100 times longer than those moving (largely) along the magnetic field. Thus, over 80% of the observable ENA flux at Europa propagates in planes nearly perpendicular to the magnetic field and contributes to the band. At Callisto, the ambient magnetospheric field is 1–2 orders of magnitude weaker than at Europa, and the vast majority of parent protons can only complete partial gyrations within the atmosphere. As a result, the parent protons with pitch angles near 90° are less heavily “favored” for ENA production over the field-aligned particles at Callisto, compared to the case at Europa. Hence, only about 50%–60% of the total ENA flux leaving Callisto's atmosphere contributes to the band. Comparing ENA emissions in uniform versus draped fields, Haynes et al. (2023) found that the (partial) deflection of impinging parent ions by the field perturbations reduces the intensity in the band of elevated ENA flux at both moons regardless of the longitude on the detector sphere (Haynes et al., 2023).

Because they capture all of the detectable ENAs emitted from Europa's or Callisto's atmosphere, the global maps of ENA flux from Haynes et al. (2023) cannot be directly compared to actual ENA images taken by a spacecraft detector. An ENA detector is point-like on the length scales of the plasma interaction (e.g., Europa's or Callisto's radius) and has a limited FOV. Thus, at a given position, such an instrument would capture only a small fraction of the ENA flux which contributes to the global emission maps. Therefore, the physics encoded in the ENA emissions (readily accessible in the maps of Haynes et al. (2023)) are deeply “encrypted” within ENA images of Europa and Callisto, to be captured during the JUICE mission (Galli et al., 2022; Grasset et al., 2013; Tosi et al., 2024). Hence, the analysis of such images requires a template for “decrypting” the physics contained in the observed ENA emissions.

Tippens et al. (2024) combined the three-dimensional structure of the draped fields from AIKEF and a particle tracing tool for the energetic parent ions to assemble synthetic ENA images for the upstream conditions observed during Cassini's TA flyby of Titan. These authors employed a “backtracing” approach for calculating synthetic ENA images: their model initializes energetic parent ions at the positions where they emit ENAs into the detector, and evolves their trajectories backward in time (using a *negative* timestep). Thus, their model does not calculate any ion trajectories that, for example, would never enter Titan's atmosphere and emit an ENA toward the detector. Therefore, this approach is much more computationally efficient than, for example, the global detector model of Haynes et al. (2023). After identifying which parent ion trajectories emit ENA flux into the detector, the model of Tippens et al. (2024) computes their contributions to the synthetic ENA image by treating their charge exchange interactions with Titan's upper atmosphere. The influence of field line draping on the structures in the synthetic ENA images produced for TA was found to depend strongly on the detector's viewing geometry: the modifications introduced by draping are visible only from certain vantages, with no morphological differences in the synthetic ENA images between uniform and draped fields for others. That is, *if and how* the draping of Saturn's magnetospheric field around Titan's ionosphere is visible in synthetic ENA images depends on the location of the imaging instrument and the pointing of its boresight vector (Tippens et al., 2024).

To date, no synthetic ENA images have been generated for Europa or Callisto. In order to provide a forecast of upcoming ENA observations, we therefore proceed analogous to Tippens et al. (2024) and combine a backtracing tool for the energetic parent ions with the three-dimensional electromagnetic fields from the AIKEF hybrid model. For numerous viewing geometries at both moons, we compare synthetic ENA images generated for uniform and draped electromagnetic fields. In this way, we constrain which positions and pointings of an ENA detector may allow for a global characterization of the field perturbations in the vicinities of Europa and Callisto. More specifically, the goal of this study is twofold: (a) we aim to catalog the morphology of atmospheric ENA emissions to be detected by an ENA imager at Europa and Callisto, identifying the role of field line draping in shaping these images. (b) At both moons, we shall constrain the variability of the synthetic ENA images as a function of distance to the center of Jupiter's plasma sheet.

The outline of this manuscript is as follows: in Section 2, we provide an overview of the parameters used in AIKEF to emulate the draped fields near Europa and Callisto. We also describe the model employed to calculate synthetic ENA images at both moons. In Section 3, we discuss the morphology of the features seen in our synthetic ENA images, investigating how Europa's and Callisto's non-uniform electromagnetic environments map into these images. We also probe the dependence of this effect on the viewing geometry. Finally, in Section 4, we conclude with a brief summary of our major findings.

## 2. Modeling ENA Emissions at Europa and Callisto

In Section 2.1, we provide a brief overview of the parameters used in the AIKEF hybrid model to calculate the draped electromagnetic fields near Europa and Callisto. In Section 2.2, we describe the model used for generating synthetic ENA images at these moons. Throughout this study, we employ the Cartesian Satellite Interaction System (SIS) with coordinates  $\mathbf{r} = (x, y, z)$  at each moon. This system originates at the center of Europa or Callisto, with the following unit vectors:  $\hat{\mathbf{x}}$  is aligned with the direction of corotational flow in our model,  $\hat{\mathbf{z}}$  is perpendicular to  $\hat{\mathbf{x}}$  and (approximately) aligned with Jupiter's spin axis, and  $\hat{\mathbf{y}} = \hat{\mathbf{z}} \times \hat{\mathbf{x}}$  bears roughly toward Jupiter, completing the system. The symbol  $R$  represents the radius of the respective moon, that is,  $R = R_C$  at Callisto and  $R = R_E$  at Europa.

### 2.1. Three-Dimensional Model of Europa's and Callisto's Electromagnetic Environments

In order to construct synthetic ENA images at Europa or Callisto, the 3D structure of these moons' electromagnetic environments must be known. We use the AIKEF hybrid model (Müller et al., 2011) to calculate the perturbations to the electric and magnetic fields near Europa and Callisto, generated by the interaction between the moons and the impinging thermal magnetospheric plasma. AIKEF has an extensive history of application at both Callisto (Haynes et al., 2023; Liuzzo et al., 2015, 2016, 2017, 2018, 2019a, 2019b, 2022, 2024) and Europa (Addison et al., 2021, 2022, 2023, 2024; Arnold, Liuzzo, & Simon, 2020; Arnold, Simon, & Liuzzo, 2020; Arnold et al., 2019; Breer et al., 2019; Haynes et al., 2023). For this study, we use the exact same electromagnetic field configurations as the preceding analysis of the global ENA emission morphology at Europa and Callisto by Haynes et al. (2023): these authors considered the moons' electromagnetic environments at the center of the Jovian magnetospheric plasma sheet as well as at maximum distance below it. At both of these locations, they took into account the draped fields from AIKEF and a “baseline” scenario that treats the fields near each moon as uniform. In the latter case, the magnetic field is set to the uniform magnetospheric background field  $\mathbf{B}_0$  at the moon's position, and the electric field is given by  $\mathbf{E}_0 = -\mathbf{u}_0 \times \mathbf{B}_0$ , where  $\mathbf{u}_0$  denotes the ambient plasma flow velocity. Thus, four distinct model scenarios for the fields are considered at both Europa and Callisto. The magnetospheric upstream conditions for these setups are summarized in Table 1 of Haynes et al. (2023). For a detailed justification of the chosen model parameters, we refer the reader to Section 2.1 in that work. Visualizations of the draped fields for each AIKEF scenario are shown and discussed in Section 3.1 of Haynes et al. (2023).

The dependence of the magnetospheric thermal ion density  $n_0$  on distance to the center of Jupiter's plasma sheet follows a Gaussian distribution (e.g., Bagenal & Delamere, 2011). As a result, the upstream plasma density at both moons is smaller at their maximum distance below the Jovian plasma sheet, compared to the center. The bulk velocity  $\mathbf{u}_0$  of the impinging plasma is aligned with the (+x) axis, and it has a magnitude of  $|\mathbf{u}_0| = 100$  km/s at Europa and  $|\mathbf{u}_0| = 192$  km/s at Callisto (see Kivelson et al. (2004) and Section 2.1 of Haynes et al. (2023)). The magnetic environment of both moons may be modified by an induction signal from a conducting subsurface ocean (Europa, Callisto) or ionosphere (Callisto). In AIKEF, the induced field is treated as a dipole centered at the moon, and the strength of the induced magnetic moment is proportional to the horizontal component of  $\mathbf{B}_0$  (see discussion of Equation 1 in Haynes et al. (2023)). When Europa and Callisto are at maximum distance from the center of Jupiter's plasma sheet,  $\mathbf{B}_0$  possesses three nonzero components, and the induced field is at its strongest. In contrast, when each moon is at the center of the Jovian plasma sheet, the ambient magnetospheric field  $\mathbf{B}_0$  is nearly anti-parallel to Jupiter's spin axis and no induced magnetic moment is included in our model.

At both moons, the atmospheric neutral density as a function of altitude is described by a barometric law for each constituent. The AIKEF model also assumes Europa's and Callisto's neutral envelopes to possess a ram-wake asymmetry: at both moons, the density of the neutral gas peaks at the ramside apex. At Europa, we include only the O<sub>2</sub> component observed to dominate the atmosphere below altitudes of several hundred km (Plainaki

et al., 2018; Roth et al., 2016; Vorburger & Wurz, 2018). We use a scale height of 100 km and a surface density of  $5.5 \cdot 10^{14} \text{ m}^{-3}$  at the ramside apex, which yields a column density consistent with that derived from UV observations (Hall et al., 1995, 1998; Roth et al., 2016). Cervantes and Saur (2022) found that the additional, localized bulge of elevated H<sub>2</sub>O density around the moon's subsolar or ramside apex (Roth, 2021) only introduces very subtle modifications to Europa's electromagnetic environment. Besides, the global ENA emission model of Haynes et al. (2023) revealed that the inclusion of this H<sub>2</sub>O component does not generate any morphological changes to the global ENA emission pattern. For this reason, the atmospheric H<sub>2</sub>O bulge is not included in our model. At Callisto, we incorporate both the observed CO<sub>2</sub> and O<sub>2</sub> components of the atmosphere (Carlson, 1999; Cunningham et al., 2015). To obtain column densities within the observed range, we use a surface density (at the ramside apex) of  $1.0 \cdot 10^{15} \text{ m}^{-3}$  for molecular oxygen and  $4.0 \cdot 10^{13} \text{ m}^{-3}$  for carbon dioxide, both with a scale height of 230 km (for further details, see also Liuzzo et al., 2015). Our chosen value for Callisto's O<sub>2</sub> column density is approximately within a factor of 2 to a recent deduction using observations of the moon's optical aurorae by the Hubble Space Telescope (de Kleer et al., 2023). In the AIKEF model, Europa's atmosphere is partially ionized by electron impacts, whereas Callisto's ionosphere is generated through a combination of solar UV ionization and electron impact ionization (see Haynes et al., 2023, and references therein).

The model domain at Callisto is a cube centered at the moon with edges spanning  $-15R \leq x, y, z \leq 15R$ . At Europa, we use a cuboid which extends  $-8R \leq x \leq 22R$  in the corotation direction,  $-10R \leq y \leq 10R$  along the Europa-Jupiter line, and  $-30R \leq z \leq 30R$  in the north-south direction. The extension of the model domain for each baseline case (using uniform fields) is identical to that of the AIKEF domain at the respective moon.

## 2.2. Generating Synthetic ENA Images at Callisto and Europa

In order to generate synthetic ENA images that can guide the planning of observations, we must calculate the ENA flux entering a point-like (on length scales of the plasma interaction) spacecraft detector with a finite field of view (FOV) for different electromagnetic environments at each moon. The model applied by Haynes et al. (2023) to calculate the *global* ENA emission morphology is not suitable for this endeavor; the number of ENAs passing through any specific point (e.g., a spacecraft detector) in their simulation domain is near-zero. Thus, that model would require runtimes on the order of several months to obtain even a single, smoothly resolved synthetic ENA image. For this reason, we implement a “backtracing” method which initializes parent protons at the point where they would emit an ENA into the detector, and evolves their trajectories backwards in time, that is, with a *negative timestep* ( $\Delta t < 0$ ). Such an approach has already been used to calculate synthetic ENA images that replicate key features of the Cassini INCA observations from the spacecraft's first Titan flyby, TA (Tippens et al., 2024). Our model framework adapts these authors' approach for use at Europa and Callisto. Because this method avoids calculating the trajectories of energetic parent protons that never enter the moon's atmosphere or bear toward a pixel of the ENA detector, it can rapidly generate synthetic ENA images. In the following, we provide an overview of this model's major features. For a more detailed discussion of individual model elements, the reader is referred to Tippens et al. (2024).

The energy range (for H: 0.5 – 300 keV) of the JENI instrument is already available in the peer-reviewed literature (Galli et al., 2022); however, parameters such as the angular range of the FOV or the number of pixels in each direction are not yet exactly specified (Mitchell et al., 2016). Therefore, the properties of the ENA detector in our model are similar to those of the Ion and Neutral Camera (INCA) that was mounted upon the Cassini spacecraft, which has flight-proven, publicly available capabilities (Krimigis et al., 2004; Mitchell et al., 1993). In the model, the detector surface is represented by a segment of a spherical cap, where the FOV spans 90° in azimuth and 120° in elevation. Each pixel has a different line of sight (LOS) that extends radially outward. The position and orientation of the boresight vector and four corner pixels uniquely specify the pointing of the model detector. The ENA flux detected by any pixel on the detector is given by the sum of the ENA flux contributions emitted by individual parent protons along its associated LOS.

Since ENAs travel (roughly) along straight lines, any parent proton that contributes to the ENA image must possess a velocity vector which points toward the detector along a LOS at a certain point in time. Any LOS that does not intersect the atmosphere is assigned zero ENA flux. For pixels that face the atmosphere, the LOS is extended until it encounters the far boundary of the neutral envelope or the surface of the moon. Figure 1 displays a schematic of this backtracing technique, with the straight black line illustrating a LOS. For a LOS which intersects the surface of the moon, only the ENAs produced along the LOS segment *between* the moon and the

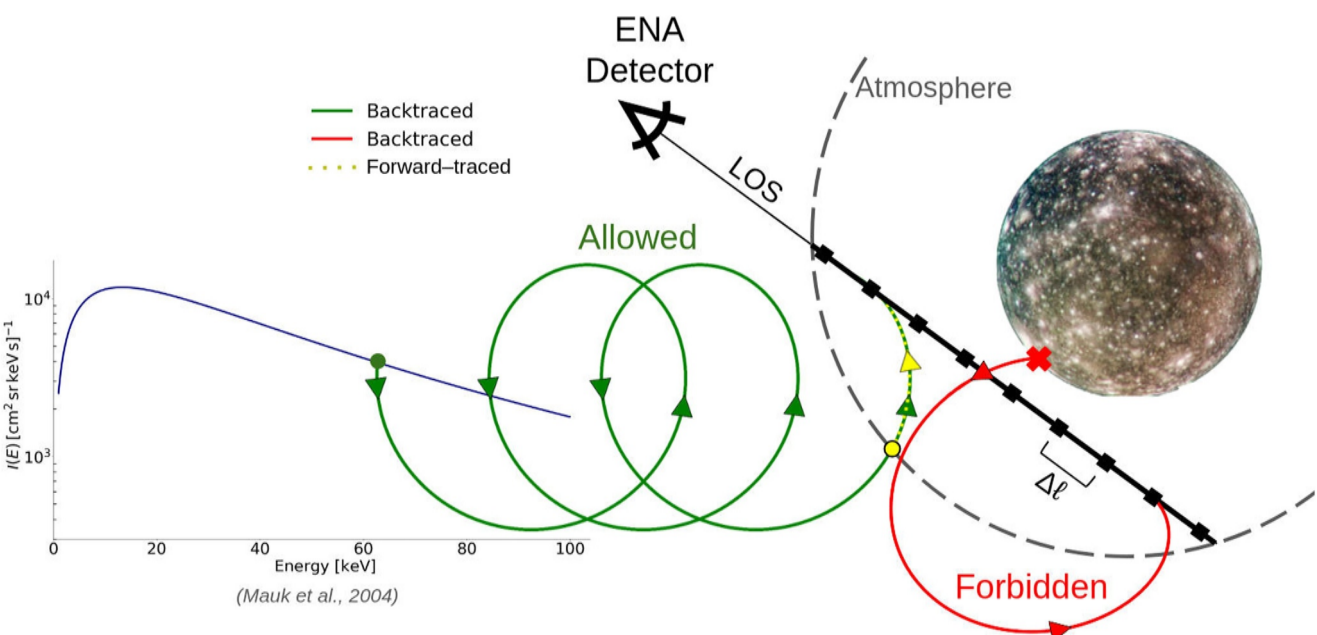


**Figure 1.** Depiction of the backtracing model used to calculate synthetic ENA images of the magnetosphere-atmosphere interactions at Europa and Callisto (adapted from Tippens et al. (2024)). The eye-like element corresponds to the ENA detector. The black line emanating from the ENA detector represents a sample line of sight (LOS). The interval of the LOS within the moon's atmosphere (thick black line) is discretized into segments of length  $\Delta\ell$ . The red and green curves represent respective “forbidden” and “allowed” trajectories of parent protons backtraced from a LOS segment to determine the ambient intensity, with the arrowheads denoting their instantaneous velocity vectors. The observed intensity distribution  $I(E)$  of the ambient energetic proton flux (blue curve) is sampled at the energy  $E$  of the parent proton (with an allowed trajectory) when it reaches the uniform fields outside of the moon's interaction region. Subsequently, any proton with an allowed trajectory is returned to the top of the atmosphere (yellow dot) and traced forward in time to calculate ENA generation (yellow, dotted line).

detector can contribute to the flux into the corresponding pixel. As shown in Figure 1, the interval of each LOS within the atmosphere is discretized into segments of length  $\Delta\ell$ . The value of  $\Delta\ell$  is chosen to be shorter than the atmospheric scale height at the respective moon: we set  $\Delta\ell = 0.015R$  in both cases (where  $R = R_E$  at Europa and  $R = R_C$  at Callisto). This value corresponds to a segment length of  $\Delta\ell = 23.4$  km at Europa and  $\Delta\ell = 36.2$  km at Callisto. Since the atmospheric scale height in our model is  $230$  km =  $0.095R$  at Callisto and  $100$  km =  $0.064R$  at Europa,  $\Delta\ell$  comfortably resolves this length scale at both moons.

ENA imaging instruments such as INCA and JENI cannot provide each ENA's exact kinetic energy due to downlink limitations. Their full sensitivity range is rather decomposed into several energy channels, usually spanning tens of keV (e.g., Krimigis et al., 2004; Mitchell et al., 2005). The intensity of atmospheric ENA emissions is maximized at parent proton energies  $E$  between 10 and 40 keV at Callisto and between 40 and 70 keV at Europa. At both moons, the ENA flux emitted from the atmosphere falls off above and below these energies (Haynes et al., 2023). Building upon this result, our model detector measures the ENA flux in a (hypothetical) energy channel  $5 \text{ keV} \leq E \leq 75 \text{ keV}$  that captures the peak energy of ENA emissions at *both* Europa and Callisto. Using the same energy range at both moons also allows for direct comparison of the synthetic ENA images, thereby facilitating the identification of common physical processes that shape the image morphology. Since the gyroradius of a proton grows by a factor of  $\sqrt{15}$  from 5 keV to 75 keV, we segment this energy channel into eight linearly equidistant parent proton (and associated ENA) energies  $E_j$  such that  $E_j = 5 \text{ keV} + j \cdot 10 \text{ keV}$ , where  $j \in \{0, \dots, 7\}$ . The initial energy  $E_j$  assigned to each backtraced parent proton (mass  $m_p$ ) when launched from a LOS determines its speed  $|\dot{\mathbf{r}}| = \sqrt{2E_j/m_p}$  at the launch point. Because an ENA emitted into the detector has the same velocity vector as its parent proton at the moment of charge exchange, the backtraced proton is given an initial velocity  $\dot{\mathbf{r}}$  that points toward the detector. Charge exchange interactions only result in ENA production if the energetic parent ion is singly charged. Analogous to Haynes et al. (2023), we consider only ENA production by energetic magnetospheric protons. Given the large number of cases that need to be analyzed for protons alone, we refrain from including the two heavier ion species (sulfur and oxygen) in this study.

From the center of each LOS segment  $\Delta\ell$  within the atmosphere, eight parent protons at energies  $E_j$  (where  $j \in \{0, \dots, 7\}$ ) are launched and traced backwards in time, that is, with a negative timestep  $\Delta t < 0$ . The backtracing process does not consider any interactions between protons and neutral gas, and no ENAs are produced yet. This procedure is used exclusively to identify parent protons that contribute to the synthetic ENA image. The magnitude of their contributions is determined in a subsequent step of the model. Parent protons are traced until they either (a) impact the moon, or (b) reach the undisturbed plasma at the outer faces of the model domain. Fate (a) represents a “forbidden” trajectory; when traced forward in time ( $\Delta t > 0$ ), such a parent proton would have to travel through the solid body of the moon in order to reach its launch point on the LOS (e.g., red trajectory in Figure 1). Ions which take forbidden trajectories are deleted from the model and contribute no flux to the synthetic ENA image. In other words, the model does not consider ENA generation through surface sputtering (Pontoni et al., 2022; Szabo et al., 2024). At both moons, a backtraced proton may travel along Jovian magnetospheric field lines out of the local interaction region, bounce at its mirror point, and return to Europa's or Callisto's immediate environment. In the forward-tracing picture, the distance downstream (i.e., in positive  $x$  direction) where bouncing protons at energies  $E \leq 75$  keV would return to the interaction region is larger than  $30R_C$  at Callisto (Liuzzo et al., 2019b) and exceeds  $10R_E$  at Europa (Nordheim et al., 2022; Paranicas et al., 2009). Therefore, such bouncing protons cannot hit the moon's surface upon return and become “forbidden.” Rather, they fall into category (b).

Fate (b) corresponds to an “allowed” trajectory, that is, a parent proton which propagates forward in time ( $\Delta t > 0$ ) from the ambient magnetospheric plasma and reaches its launch point on the LOS (e.g., green trajectory in Figure 1). In the considered energy range, the gyroradii  $r_g$  for energetic parent protons at Europa always satisfy  $r_g \ll R_E$ . The largest gyroradii of parent protons in our model ( $r_g \approx 4.10 R_C$ ) occur at  $E_7 = 75$  keV in the weak magnetospheric field near Callisto ( $|\mathbf{B}_0| = 4$  nT) when located at the center of Jupiter's plasma sheet. Even this value of  $r_g$  is less than half of the distance between the outer faces of the model domain and the surface of the moon ( $14 R_C$ , see also Section 2.1 and Haynes et al., 2023). Thus, a parent proton that reaches an outer face of the model domain at Europa or Callisto cannot return to hit the surface—neither through gyration nor through bouncing—and possesses an allowed trajectory.

The energetic magnetospheric protons in the model are treated as macroparticles, each of them representing the differential flux carried by a large number of real protons. For each allowed proton trajectory, the energetic ion spectrum  $I(E)$  observed outside of the moon's interaction region (blue curve in Figure 1) is sampled at the energy  $E$  of the parent proton when reaching the outer faces of the model domain. In general, the value of  $E$  is different from the proton's energy  $E_j$  at launch: along its trajectory, the particle is accelerated by the fields. We adopt the approach of Haynes et al. (2023), Addison et al. (2021, 2022), and Liuzzo et al. (2022) and use the spectra  $I(E)$  observed by the Galileo and Juno spacecrafts during their flybys of both moons. Paranicas et al. (2002) give the ambient energetic proton spectra sampled near Europa during the E12 and E26 flybys. These encounters occurred when the moon was at the center of and near maximum distance below the Jovian plasma sheet, respectively. When Callisto is located at the center of the sheet, we utilize the energetic proton spectrum from Mauk et al. (2004), labeled G8 PS/A in their study. At Callisto's maximum excursion below the sheet, we use the same spectrum downsampled by a factor of 10 at all energies (for further justification, see Haynes et al., 2023; Liuzzo et al., 2022).

Galileo measured the pitch angle distribution (PAD) of energetic protons outside of Europa's interaction region, and Mauk et al. (2004) determined it to be isotropic to within 25%. However, Juno measurements of the proton PAD at Europa's orbit revealed a field-aligned distribution, with about 50% more flux at pitch angles of  $\alpha = 0^\circ$  or  $\alpha = 180^\circ$  than at  $\alpha = 90^\circ$  (Sarkango et al., 2023). The global ENA model of Haynes et al. (2023) found that the intensity distribution of ENA flux through a spherical detector around Europa remains qualitatively unchanged when including such a field-aligned PAD instead of an isotropic PAD. Their results show that the effect of the anisotropic PAD is largely quantitative, altering the emission pattern by no more than 25% at any location on the detector sphere. At Callisto's orbital distance, Galileo observations show that the energetic proton PAD for  $5 \text{ keV} \leq E \leq 75 \text{ keV}$  is largely isotropic (Mauk et al., 2004); this is further corroborated by Juno observations of the  $E = 117 \text{ keV}$  proton PAD in the same region (Shen et al., 2022). In our study, we treat the PAD of the impinging protons at both moons as isotropic. However, investigating the influence of anisotropies in the PAD on synthetic ENA images may constitute a valuable follow-up study.

Each backtraced parent proton with an allowed trajectory is assigned an initial differential flux  $J_I = I(E)$  by sampling the ambient distribution (blue curve in Figure 1). To calculate such a parent proton's production of ENAs, we follow its (previously calculated) trajectory from the outer faces of the model domain to the top of the

moon's atmosphere at  $|\mathbf{r}| = 2R$  (yellow point in Figure 1) in *forward time*, that is, with  $\Delta t > 0$ . Only a tiny fraction of the atmospheric neutral gas is located above this altitude, and hence, ENA emissions at  $|\mathbf{r}| > 2R$  can safely be neglected (Haynes et al., 2023). For an isotropic PAD, the macroparticle's flux  $J_I$  at the outer faces of the model domain is related to its flux at the top of the atmosphere  $J_\tau$  via

$$J_\tau = \frac{E_\tau}{E_I} J_I, \quad (1)$$

where  $E_I$  and  $E_\tau$  are its energies at these two locations (Haynes et al., 2023; Kollmann et al., 2019; Tippens et al., 2024). This relationship follows from the conservation of phase space density in collisionless environments (Liouville's Theorem), that is, it is valid as long as the proton macroparticle travels *outside* of Europa's or Callisto's atmosphere. Equation 1 is also applied to update a parent proton's differential flux when gyration causes it to veer out of and subsequently re-enter the atmosphere. For example, when Callisto is located near the center of the Jovian plasma sheet, large gyroradii allow the parent protons to leave and re-enter the moon's neutral envelope many times (see Figure 13 in Haynes et al. (2023)).

With the parent proton's differential flux (i.e., its numerical "weight")  $J_\tau$  at the top of the atmosphere determined by Equation 1, we subsequently model its production of ENAs. This step relies on the highly forward-scattered nature of charge exchange: in the energy range considered, a proton macroparticle loses only around 1 eV during such an interaction (e.g., Lindsay & Stebbings, 2005), a mere 0.02% of even the smallest considered energy at launch ( $E_0 = 5$  keV). Thus, energy loss due to charge exchange does not appreciably change a proton macroparticle's trajectory, and the trajectory backtraced from the launch point ( $\Delta t < 0$ ) is identical to the proton's forward-traced trajectory as it generates ENAs in the atmosphere ( $\Delta t > 0$ ). Starting from the top of the atmosphere (yellow dot in Figure 1), we follow the parent proton with a positive timestep ( $\Delta t > 0$ ) along its path within the neutral envelope (dotted yellow trajectory segment in Figure 1) to calculate the attenuation  $\Delta J$  of its differential flux  $J$ , described by

$$\Delta J = -J \sigma(E) n_n(\mathbf{r}) |\Delta s|, \quad (2)$$

analogous to the approach of Wulms et al. (2010), Kabanovic et al. (2018), Tippens et al. (2022, 2024) and Haynes et al. (2023). In Equation 2,  $n_n(\mathbf{r})$  is the neutral density at the proton's position  $\mathbf{r}$ , the step length reads  $\Delta s = \dot{\mathbf{r}} \Delta t$ , and  $\sigma(E)$  is the energy-dependent cross section for charge exchange between protons and atmospheric neutrals (Lindsay & Stebbings, 2005).

Along the segment of the parent proton's trajectory within the atmosphere, its numerical weight  $J$  is continuously attenuated according to Equation 2. One ENA is produced during each timestep  $\Delta t > 0$ , with the ENA "yield" (i.e., differential flux represented by the ENA) in each timestep given by  $Y = -\Delta J$  (Haynes et al., 2023). Each ENA is created with a velocity vector equal to the momentary velocity of the parent proton. The ENA produced when the parent proton ultimately returns to its launch point is the lone one emitted along the chosen LOS into the detector. Only this ENA contributes to the synthetic image; the ENAs produced earlier are discarded. We use the same atmospheric O<sub>2</sub> profiles for ENA generation as included in AIKEF at each moon (see Section 2.1). Analogous to Haynes et al. (2023), the ENA production model does not incorporate charge exchange between energetic protons and the CO<sub>2</sub> component of Callisto's atmosphere; the CO<sub>2</sub> column density is a factor of 25 below that of molecular oxygen (Carlson, 1999). Since the cross sections for charge exchange with CO<sub>2</sub> are only a factor of 2–3 larger than those for O<sub>2</sub> at a given energy (Lindsay et al., 2005), our model does not take into account the CO<sub>2</sub> contribution to the ENA images. Subsequent reionization and renaturalization of the ENAs after their creation is not considered in our model. Since several authors were able to reproduce the INCA observations from the TA Titan flyby without treating this effect (Kabanovic et al., 2018; Tippens et al., 2024; Wulms et al., 2010), we defer such an expansion of the model to a future study.

Analogous to Tippens et al. (2024), the total ENA flux into the pixel at the base of each LOS is determined by summing the contributions from each parent proton energy  $E_j$  at each segment  $\Delta \ell$ , and then summing the contributions for all segments along that LOS (see Equations 7 and 8 in that study). This procedure is carried out for each pixel. Finally, the synthetic ENA image is constructed like a mosaic using the calculated ENA flux emitted into each individual pixel. The process to generate a synthetic ENA image is summarized by the flowchart in Figure 2. To facilitate comparison between the synthetic ENA images and actual observations by a spacecraft

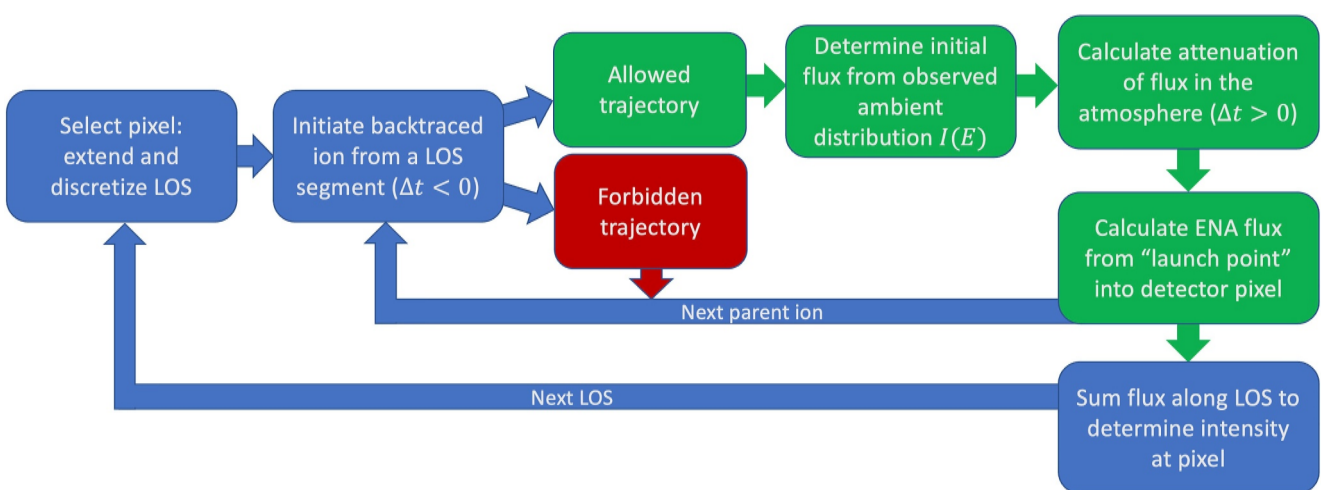


**Figure 2.** Logical structure of the backtracing model used to calculate synthetic ENA images at Europa and Callisto (adapted from Tippens et al. (2024)).

imager, we carry out the same two post-processing steps on the synthetic images as Tippens et al. (2024). First, the images are downscaled to the  $32 \times 32$  pixel grid of the INCA detector, corresponding to an angular resolution of  $3.75^\circ \times 2.81^\circ$  (e.g., Krimigis et al., 2004). The angular resolution of the detector in our model is  $1^\circ$  in both azimuth and elevation. The downscaling process mimics the nature of the larger pixels on a real ENA detector: unlike the pixels in our model, each pixel of an actual instrument can detect incoming ENAs within a small cone of velocity vectors around the associated LOS (see Section 2 of Tippens et al. (2024), for details). While the angular resolution of JENI is not yet available in the peer-reviewed literature, the targeted value of  $2^\circ$  per pixel is substantially higher than that of INCA (Mitchell et al., 2016). Since the synthetic images are generated at an angular resolution well below even this targeted value, it is readily possible to downscale our results onto the pixel grid of JENI once its parameters are available. The downscaling procedure does not introduce any morphological changes to the synthetic ENA images, but only slightly blurs them.

Second, a point spread function (PSF) is applied to account for the slight “bleedover” of the ENA flux emitted toward a certain pixel into adjacent pixels. This effect is caused by scattering of incident ENAs from the foils within the instrument (Krimigis et al., 2004). Due to its thinner foils, this effect is expected to be significantly less for JENI than for INCA (Mitchell et al., 2016). For the INCA instrument, the PSF is a product of two Gaussian distributions specified by the standard deviations in azimuthal and elevational directions (Krimigis et al., 2004). Within the range of values available in the literature, the choice of these standard deviations has little influence on the features visible in the synthetic ENA image: the PSF only slightly smears out the ENA signal across adjacent pixels (see also Tippens et al., 2024). In this study, we use values for the standard deviations provided by Dialynas et al. (2013); see also Table 2 in Tippens et al. (2024).

For Europa and Callisto, we generate a set of synthetic ENA images sampling a multitude of viewing directions for uniform and draped fields, both at the center and at maximum distance below Jupiter's magnetospheric plasma sheet. We consider six detector positions, all located at a distance of  $3R$  from the center of each moon, with the boresight vector pointing radially inward: the detector is placed above the upstream  $(-3R, 0, 0)$  and downstream  $(3R, 0, 0)$  apices, the Jupiter-averted  $(0, -3R, 0)$  and Jupiter-facing  $(0, 3R, 0)$  apices, and the north  $(0, 0, 3R)$  and south  $(0, 0, -3R)$  poles. When Europa and Callisto are at the center of the Jovian plasma sheet, the magnetospheric background field  $\mathbf{B}_0$  is taken to be southward (see Section 2.1). In this case, the detectors at  $(0, 0, \pm 3R)$  look along or anti-parallel to  $\mathbf{B}_0$ , and the boresight vectors of the other four detectors are oriented perpendicular to  $\mathbf{B}_0$ . In contrast, when each moon is at its maximum distance below the center of the Jovian plasma sheet, the ambient field  $\mathbf{B}_0$  possesses non-negligible components along all three axes of the SIS. Due to the nearly perpendicular inclination of  $\mathbf{B}_0$  against the north-south axis when Callisto is at maximum distance below the sheet, we consider four additional viewing geometries relative to  $\mathbf{B}_0$  in this case. These four model detectors are again positioned at a distance of  $3R$  from the center of Callisto, looking radially toward its center. In two of these setups, the detector is positioned on the straight line through the center of the moon that is parallel to  $\mathbf{B}_0$ ; the

detector's boresight is oriented parallel or anti-parallel to  $\mathbf{B}_0$ . In the other two setups, the detector is contained in the plane through the center of Callisto that is perpendicular to  $\mathbf{B}_0$ : specifically, we place the detector on the intersection of this plane and the  $y = 0$  plane. At Europa, we do not consider the analogous detector configurations since the ambient field  $\mathbf{B}_0$  remains southward to within  $28.5^\circ$  even at maximum distance below the plasma sheet.

Because the path length  $|\Delta s|$  in Equation 2 is proportional to the timestep ( $\Delta s = \dot{\mathbf{r}} \Delta t$  where  $\Delta t > 0$ ), the choice of  $\Delta t$  maps into the intensity of ENA emissions in the synthetic images. Our model utilizes the *same* timestep everywhere within the atmosphere: this ensures that the “brightness” of the synthetic ENA image is scaled by the same factor  $\Delta t$  at each pixel. Due to the degree of freedom introduced by the choice of  $\Delta t$ , the absolute “brightness” of our synthetic ENA images cannot be determined through this model. However, since the same timestep is used everywhere inside the atmosphere, the *relative* intensities of features in the ENA images can be constrained by our method. In other words, our approach can predict the *morphology* of the ENA images expected at Europa or Callisto. Once a single ENA image has been taken by a spacecraft at either of these moons, the timestep in our model can be calibrated to reproduce the observed brightness and to make quantitative predictions of absolute fluxes for subsequent encounters. For Titan, this has been successfully demonstrated by Tippens et al. (2024). Everywhere outside the atmosphere, we apply a value of  $\Delta t = T_{g0}/100$ , where  $T_{g0} = 2\pi m_p/(e|\mathbf{B}_0|)$  is the gyroperiod of a proton in the undisturbed background field  $\mathbf{B}_0$ . Within Europa's or Callisto's atmosphere, we use a timestep of  $\Delta t = T_{g0}/1000$ . This choice ensures that the distance traveled by a proton during each timestep remains below the atmospheric scale height at either moon. Even for Callisto at the center of Jupiter's plasma sheet (where the gyroperiod is the longest), the largest possible distance traveled during a timestep,  $|\Delta s| = |\dot{\mathbf{r}} \Delta t| \approx (\sqrt{2E_7/m_p}) (T_{g0}/1000)$ , is still only about 62 km, around a quarter of the atmospheric scale height used in our model.

### 3. Results and Discussion

#### 3.1. Analysis of Synthetic ENA Images at Callisto

##### 3.1.1. Callisto at the Center of the Jovian Plasma Sheet

Figure 3 depicts synthetic ENA images at Callisto when the moon is at the center of the Jovian plasma sheet. We consider six viewing geometries, represented by the gray detector elements. Panels (a)–(f) each show the synthetic ENA images in uniform fields (left) and in draped fields (right), all with increasing detector *elevation* on the horizontal axis and decreasing detector *azimuth* on the vertical axis. This “landscape” arrangement of the image frames is consistent with the approach frequently used to display INCA observations from Cassini's Titan flybys (e.g., Brandt et al., 2012; Mitchell et al., 2005; Tippens et al., 2024), where the detector's FOV is rotated by  $90^\circ$  clockwise about the boresight from the “portrait” orientation suggested by the detector coordinate system. For each detector position, the boresight vector is aligned with an axis of the Satellite Interaction System. Figures 3a and 3d use the detector placed on the  $x$  axis at  $(\mp 3R_C, 0, 0)$ . Figures 3b and 3e display synthetic ENA images with the detector positioned along the  $y$  axis at  $(0, \mp 3R_C, 0)$ ; Figures 3c and 3f have the detector on Callisto's north-south axis, placed at  $(0, 0, \mp 3R_C)$ . The boresight vector always points radially toward the center of the moon.

In uniform fields, the synthetic ENA images taken north and south of Callisto ( $z = \pm 3R_C$ ) both show a ring of elevated ENA flux surrounding the limb of the moon (left sub-panels in Figures 3c and 3f). The left side of each image displays ENA flux emanating from the atmosphere above Callisto's disc in the  $x < 0$  half space, and the right side depicts ENA flux from the  $x > 0$  half space. The top half of the images in Figure 3c shows the FOV segment that receives flux from the Jupiter-averted half space, and the bottom half corresponds to the Jupiter-facing half space. In Figure 3f, the locations of the Jupiter-facing and Jupiter-averted half spaces are flipped, with the top half now corresponding to  $y > 0$ . The ENA flux emitted by a parent proton at a certain point on a LOS is proportional to the local atmospheric density (see Equation 2), so the highest ENA fluxes are recorded by pixels looking just outside of the moon's disc where the associated LOS column contains the most neutral gas. For such a LOS, its path length through the atmosphere is also maximized compared to one intersecting Callisto's surface or passing the disc at higher altitudes. The scale height of Callisto's atmosphere in our model is approximately  $0.1R_C$ , which would correspond to only a pixel or two in radial extent from the disc of the moon. However, these rings appear to span multiple scale heights in the images from Figures 3c and 3f: this broadening is caused by the application of the PSF, which slightly spreads the ENA flux from the pixels near the moon's surface to neighboring ones (see also Tippens et al., 2024).

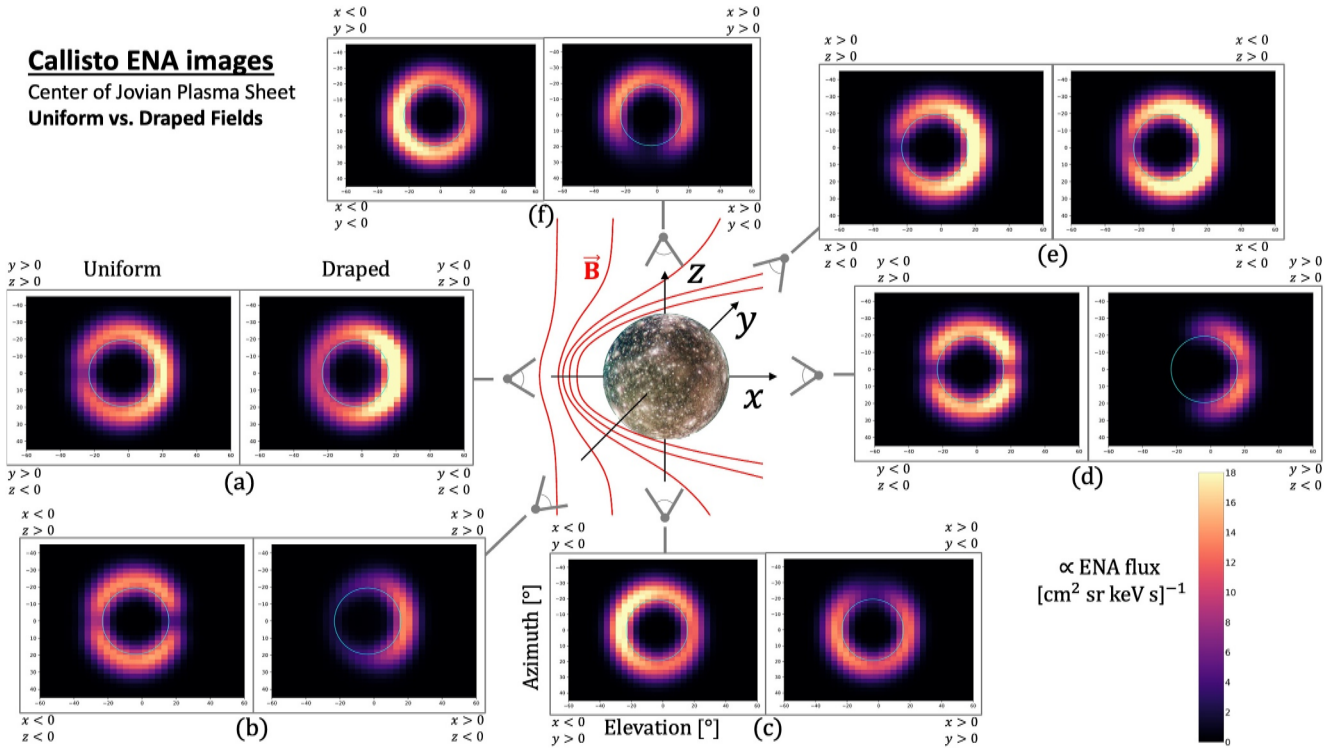


**Figure 3.** Synthetic ENA images in uniform and draped fields at Callisto when the moon is near the center of the Jovian plasma sheet. In each panel, synthetic ENA images are arranged with detector elevation on the horizontal axis and detector azimuth on the vertical axis for both uniform (left) and draped (right) magnetospheric fields. A depiction of the draped magnetic field lines near Callisto is included in red; the ambient magnetospheric field in this configuration is oriented southward. In each synthetic ENA image, the disc of the moon is represented by the light blue circle. Every panel is connected to a gray detector symbol that illustrates the viewing geometry used to create the respective images. For each of the six setups, the model detector is placed at  $2R_C$  altitude and the boresight vector points toward the center of Callisto: in panel (a), the detector points in  $(+x)$  and is located at  $(-3R_C, 0, 0)$ ; in panel (b), the detector points in  $(+y)$  and is located at  $(0, -3R_C, 0)$ ; in panel (c), the detector points in  $(+z)$  and is located at  $(0, 0, -3R_C)$ ; in panel (d), the detector points in  $(-x)$  and is located at  $(3R_C, 0, 0)$ ; in panel (e), the detector points in  $(-y)$  and is located at  $(0, 3R_C, 0)$ ; and in panel (f), the detector points in  $(-z)$  and is located at  $(0, 0, 3R_C)$ . The labels in the four corners of each panel indicate which region of the Satellite Interaction System corresponds to the associated quadrant of the images. The values of the ENA flux for our choice of  $\Delta t$  (see Section 2.2) are indicated by the colorbar in the bottom right-hand corner, where bright yellow corresponds to an intense signal, and black corresponds to none.

At the center of the Jovian plasma sheet, the magnetospheric field  $\mathbf{B}_0$  near Callisto is oriented southward (see Table 1 of Haynes et al. (2023)). At the moment of charge exchange, parent protons must have velocity vectors which are nearly aligned or anti-aligned with  $\mathbf{B}_0$  to contribute to the ring of elevated ENA flux observed from south and north of the moon (left images in Figures 3c and 3f, respectively). Since ENA generation mainly occurs within one atmospheric scale height of Callisto's surface (Haynes et al., 2023), the angle between a (uniform) magnetospheric field line and such a parent proton's velocity vector  $\xi_C$  falls within a range of approximately

$$\xi_C \in \left\{ \arcsin\left(\frac{R_C}{3R_C}\right), \arcsin\left(\frac{R_C + 0.1R_C}{3R_C}\right) \right\} \approx \{19.5^\circ, 21.5^\circ\}, \quad (3)$$

where  $0.1R_C$  is the atmospheric scale height in our model (see Section 2.1) and  $3R_C$  is the distance between the detector and the moon's center. Hence, the lines of sight which constitute the ring in both Figures 3c and 3f are confined between two cones with apices at the detector, axes aligned with the boresight vector, and opening angles of  $19.5^\circ$  and  $21.5^\circ$ .

Protons with velocity vectors outside this cone also produce ENAs. However, these cannot be observed by the detectors in Figures 3c and 3f. In uniform fields, parent protons contributing to the ring in Figure 3c must have pitch angles of  $\alpha \approx \xi_C$ , that is, they mainly approach Callisto from the north. Likewise, protons contributing to the ring in Figure 3f must have pitch angles of  $\alpha \approx 180^\circ - \xi_C \approx 158.5^\circ$ , indicating they approach the moon from the south. The angle  $\xi_C$  thus determines the angular size of the ring in the synthetic ENA images. In Figures 3c and 3f, the ring of high ENA flux intersects the azimuth axis (i.e., where elevation is  $0^\circ$ ) between angles of  $\pm(21^\circ - 26^\circ)$ , similar to

the value predicted by Expression 3. This estimation does not take into account the  $\mathbf{E}_0 \times \mathbf{B}_0$  drift velocity: even for parent protons at the lower bound of our energy range ( $E_0 = 5$  keV), the  $\mathbf{E}_0 \times \mathbf{B}_0$  drift speed is at least four times slower than their translation and/or gyration velocities  $\sqrt{2E_0/m_p}$  (see also Haynes et al., 2023).

In uniform fields, the ENA flux intensity within the rings in Figures 3c and 3f peaks at the upstream apex and decreases by 40%–50% moving toward the downstream apex along Callisto's Jupiter-facing and Jupiter-averted flanks. This decrease is caused by the ram-wake asymmetry in the moon's atmospheric O<sub>2</sub> density: as described by Equation 3 of Haynes et al. (2023), the O<sub>2</sub> number density peaks at the ramside apex and decreases with angular distance when moving toward the wakeside. When approaching the wakeside apex, the atmospheric density in the model drops rapidly to zero (see also Liuzzo et al., 2015, for further discussion). However, no corresponding gap in ENA flux is formed above the wakeside apex. A LOS which intersects this region also extends through portions of Callisto's atmosphere *outside* the  $z = 0$  plane where the atmospheric density does not vanish; parent protons entering such regions contribute to the ENA flux observed above the wakeside apex of the moon's disk in uniform fields (Figures 3c and 3f). Furthermore, a possible gap in ENA flux above the wakeside apex would be partially repopulated by flux from neighboring pixels through application of the PSF.

For all six viewing geometries, the ENA flux into the detector drops to zero for pixels *inside* the disc of the moon (i.e., the light blue circle; see Figure 3). The mechanism responsible for producing this depletion is distinct between ENA images taken by a detector in the  $z = 0$  plane (Figures 3a, 3b, 3d, and 3e) and those with the detector positioned at  $z = \pm 3R_C$  (Figures 3c and 3f). For the latter, the velocity vectors of any parent protons which could populate Callisto's disc with ENA flux are largely anti-aligned or aligned with the ambient magnetic field, to within 19.5° (the lower threshold for  $\xi_C$ , see Expression 3). Any hypothetical ENAs reaching the detector at (0, 0,  $\pm 3R_C$ ) within Callisto's disc would have to be produced on the opposite side of the moon, traveling inside a cone with its apex at the detector and an opening angle of 19.5°. However, such a cone is “corked” by the body of Callisto; that is, any ENAs emitted along a LOS *inside* this cone impact the moon before reaching the detector. In consequence, there is no ENA flux emitted along lines of sight which intersect Callisto's disc in Figures 3c and 3f.

In contrast, for the detector locations in the  $z = 0$  plane (left images in Figures 3a, 3b, 3d, and 3e), the boresight vectors are *normal* to the (uniform) ambient field  $\mathbf{B}_0$ . Similar to Figures 3c and 3f, the angle between a given LOS and the ambient magnetic field determines the pitch angle of the parent protons which emit ENAs along that LOS. Parent protons which intersect a LOS within a cone around the boresight (opening angle 19.5°) would have pitch angles  $\alpha$  between  $90^\circ - 19.5^\circ = 70.5^\circ$  and  $90^\circ + 19.5^\circ = 109.5^\circ$ . However, observable ENAs would have to be produced *between* Callisto and the detector. Even for a parent proton with the lowest energy considered (i.e.,  $E_0 = 5$  keV), the gyroradius  $(\sqrt{2E_0m_p} \sin \alpha)/(e|\mathbf{B}_0|)$  within this range of pitch angles is about  $(1.0 - 1.1)R_C$ , an order of magnitude larger than the atmospheric scale height. Therefore, when a proton gyrates into the atmosphere between Callisto and the detector, it does not have sufficient space to turn such that it can emit an ENA along a LOS toward the detector (largely in the radial direction). Parent protons can access the atmosphere with velocity vectors bearing toward a detector on the opposite side of the moon; however, analogous to the scenario described for the detectors located at (0, 0,  $\pm 3R_C$ ), the body of the moon “corks” the cone of lines of sight intersecting the moon's disc, blocking any ENAs produced by such protons. As a result, Callisto's disc is also depleted of ENA flux for detectors in the  $z = 0$  plane (Figures 3a, 3b, 3d, and 3e).

When draping is included for the two detectors at  $z = \pm 3R_C$  (see right side of Figures 3c and 3f), a “gap” in ENA flux is introduced to the ring in the Jupiter-averted segment of the image ( $y < 0$ ). The formation of this gap can largely be attributed to parent proton deflection by the asymmetric magnetic pile-up region near Callisto. A depiction of the enhanced magnetic field, as calculated by AIKEF, is displayed for the  $z = 0$  and  $x = 0$  planes of the SIS in Figures 4a and 4b, respectively. Figure 4a demonstrates how the pile-up region stretches to  $y \approx -2R_C$ , wrapping around the Jupiter-averted, upstream quadrant of the moon in the equatorial plane (see also Liuzzo et al., 2015, 2017). As can be seen in Figure 4b, the region of enhanced  $|\mathbf{B}|$  reaches polar latitudes in the northern and southern hemispheres and wraps around Callisto in a highly asymmetric way, mostly confined to the Jupiter-averted half space ( $y < 0$ ). When the fields are uniform, the proton population contributing to the ring of elevated ENA flux in Figures 3c and 3f propagates with largely field-aligned or anti-aligned pitch angles. In draped fields, the pile-up region diverts some of these protons away from Callisto's atmosphere; that is, it prevents a portion of the ambient proton distribution from emitting ENAs into the detector. This introduces the gap visible in the ring structure of Figure 3f. As shown in Figure 4b, Callisto's Jupiter-averted limb ( $y < 0$ ) is protected to a higher degree by the compressed field lines than the Jupiter-facing one ( $y > 0$ ). Compared to the case of uniform

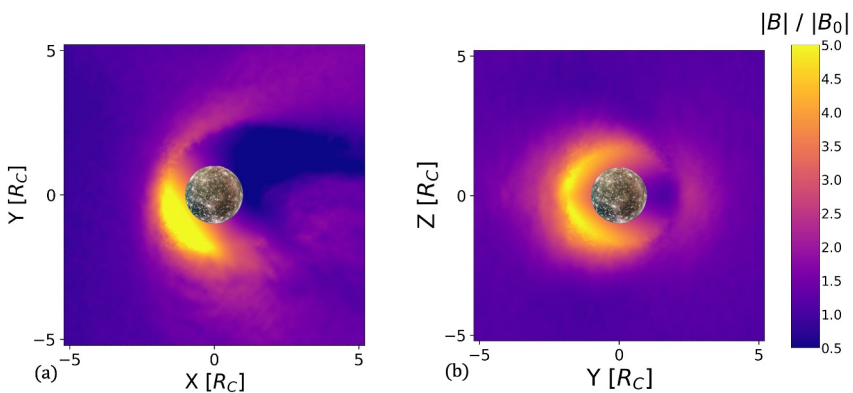


**Figure 4.** Depiction of the magnetic field magnitude  $|B|$  in the vicinity of Callisto. Panel (a) shows the  $z = 0$  plane, containing the upstream flow velocity  $\mathbf{u}_0$  and the ambient electric field vector  $\mathbf{E}_0 = -\mathbf{u}_0 \times \mathbf{B}_0$ . Panel (b) shows the  $x = 0$  plane that contains  $\mathbf{E}_0$  and  $\mathbf{B}_0$ , looking toward upstream. The magnetic field values shown by the colormaps are normalized to the ambient magnetosospheric field strength  $|\mathbf{B}_0| = 4$  nT (see Table 1 of Haynes et al. (2023)), and the colorbar on the right applies to both panels.

fields, this drives an asymmetric reduction of the ENA flux into the ring, generating the crescent-like feature seen in Figures 3c and 3f. When Callisto's plasma interaction is taken into account, the ENA flux within these crescent features is reduced by up to 25%, compared to the values recorded by these pixels in uniform fields (Figures 3c and 3f). This reduction is similar in magnitude to that of the ENA flux through a spherical detector encompassing Callisto's entire atmosphere: Haynes et al. (2023) found that field line draping diminishes the ENA flux intensity through the detector sphere by 20%–50%, depending on the location on the sphere.

We now discuss the emission features in the synthetic ENA images with boresight vectors perpendicular to the ambient magnetic field  $\mathbf{B}_0$ . Figures 3a, 3b, 3d, and 3e display our results for these cases. In these panels, the  $z > 0$  half space corresponds to the top half of the image. When the fields are uniform, a similar image morphology is visible from all four vantages: a ring of elevated ENA flux surrounds Callisto's disc, interrupted by narrow gaps in the moon's equatorial plane ( $z = 0$ ). The number and location of these gaps depend on the detector's position in the  $z = 0$  plane. As can be seen in Figures 3a and 3d, equatorial gaps in the ring of elevated ENA flux are present on both sides of the moon for the detector at  $(+3R_C, 0, 0)$ , but only one occurs (in the  $x > 0$  half space) when the detector is located upstream at  $(-3R_C, 0, 0)$ . Similarly in Figures 3b and 3e, two equatorial gaps are present when the detector is located at  $(0, -3R_C, 0)$ , but only one ( $x > 0$ ) for the detector at  $(0, +3R_C, 0)$ .

The gaps in the ring of elevated ENA flux can be attributed to “shielding” by Callisto due to the  $\mathbf{E}_0 \times \mathbf{B}_0$  drift (bearing toward downstream) and the parent protons' sense of gyration. The mechanism for this shielding is depicted for the backtracing picture in Figure 5, where energetic protons are launched with  $\Delta t < 0$  from different lines of sight that intersect Callisto's atmosphere near its limb on both sides. In Figure 5a, we consider ENA detectors positioned at  $(\pm 3R_C, 0, 0)$ , and in Figure 5b the detectors are at  $(0, \pm 3R_C, 0)$ . For the detector located downstream ( $x = +3R_C$ ), as illustrated in Figure 5a, parent protons backtraced from the LOS in the  $y < 0$  half space are near the largest negative  $y$  value of their gyration when launched. Such protons will quickly impact the moon, demonstrated by the forbidden (red) trajectory near the Jupiter-averted apex. In the forward-tracing picture, these parent protons are blocked by Callisto's surface before reaching the LOS near the moon's anti-Jovian apex with a tangential velocity vector.

Again for the detector at  $x = +3R_C$  (Figure 5a), most parent protons cannot reach a LOS connecting to the equatorial atmosphere for  $y > 0$  with a tangential velocity vector: in the backtracing picture, many such protons would impact the surface of Callisto after nearly a full gyration. Backtraced trajectories similar to the one shown for  $y > 0$  may be allowed (and emit ENA flux toward the detector at  $x = 3R_C$ ) if they intersect the LOS in the  $x < 0$  half space. However, ENA generation by such protons would occur at much higher altitudes (i.e., within much lower neutral densities) than in the example displayed. Thus, such protons emit little ENA flux into the detector. In consequence, there are equatorial gaps in the ring on both sides of the moon for the synthetic ENA image taken downstream of Callisto (Figure 3d).

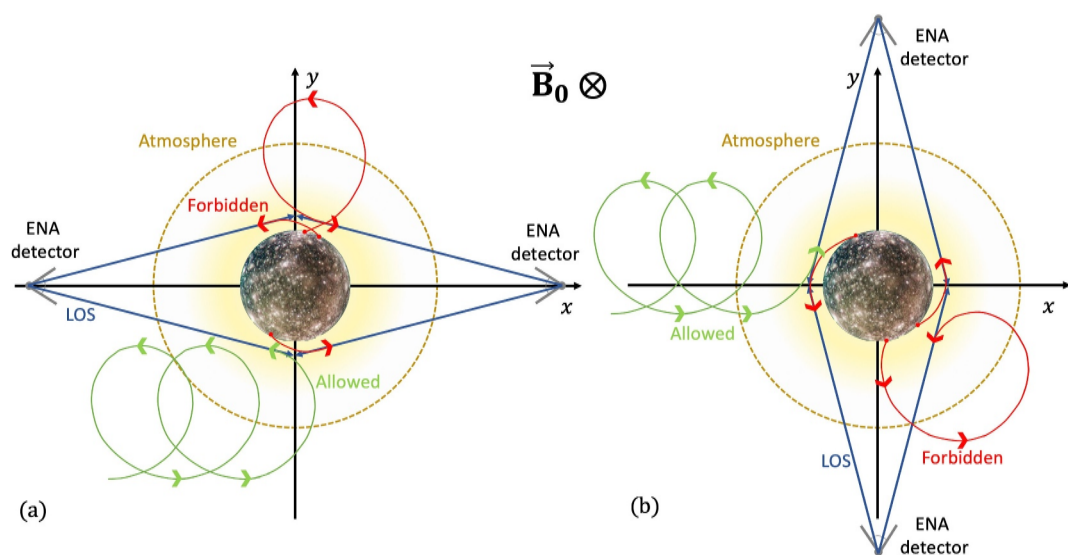


**Figure 5.** Schematic illustration of the shielding of parent protons with pitch angles  $\alpha \approx 90^\circ$  and energies  $E \approx 10$  keV by Callisto's surface, displayed in the  $z = 0$  plane. Several lines of sight (blue) are extended within this plane from the detector toward the limb of Callisto's atmosphere on either side of the moon. Backtraced parent protons are launched from a LOS and evolved with a negative timestep ( $\Delta t < 0$ ). Panel (a) illustrates the shielding for the ENA detectors positioned upstream and downstream of the moon at  $(\mp 3R_C, 0, 0)$ , as seen in Figures 3a and 3d. Panel (b) illustrates the geometry for detectors at  $(0, \mp 3R_C, 0)$ , corresponding to Figures 3b and 3e. Each of the four detectors is represented by gray elements. For the energy range considered, proton gyroradii are between  $1.1R_C$  and  $4.1R_C$  (see Table 2 in Haynes et al. (2023)).

When the detector is positioned at  $(-3R_C, 0, 0)$  and the fields are treated as uniform, an analogous process occurs for a LOS intersecting the limb of Callisto's atmosphere in the  $y > 0$  half space (see Figure 5a). In this viewing geometry, the parent protons only bear toward the detector when located near the sub-Jovian “crests” of their trajectories. Therefore, a proton backtraced from the LOS in the  $y > 0$  half space impacts the surface of the moon shortly after launch, as illustrated in the upper-left quadrant of Figure 5a. However, for the same detector position, a LOS connecting to Callisto's limb in the  $y < 0$  half space is *not* shielded by the moon. As demonstrated by the allowed (green) trajectory backtraced from such a LOS in Figure 5a, such parent protons only approach (but do not hit) the surface of Callisto as they emit ENAs along the LOS. Thus, the ring of elevated ENA flux observed at  $(-3R_C, 0, 0)$  only has a single equatorial gap in the  $y > 0$  half space (see Figure 3a).

For uniform fields, the same dichotomy in the number of gaps is visible for the synthetic ENA images taken at  $(0, \pm 3R_C, 0)$ , as seen in Figures 3b and 3e. When the detector is positioned at  $y = -3R_C$ , parent protons backtraced from a LOS in the  $x < 0$  half space quickly gyrate into Callisto, despite being carried toward upstream by the (small)  $\mathbf{E}_0 \times \mathbf{B}_0$  drift velocity. In the  $x > 0$  half space, backtraced parent protons may complete nearly a full gyration before impacting the moon during their drift toward upstream. Trajectories displaced slightly farther toward  $y < 0$  than our sample trajectory may avoid Callisto while making a weak contribution to the ENA flux into the associated pixel. For a detector located at  $y = +3R_C$ , the sample proton backtraced from the LOS in the  $x > 0$  half space completes only a small fraction of a gyration before impacting Callisto's surface due to the  $\mathbf{E}_0 \times \mathbf{B}_0$  drift and its sense of gyration. In turn, the proton backtraced from the LOS in the  $x < 0$  half space drifts away from the moon on an allowed trajectory (green), illustrating why the ring of elevated ENA flux in Figure 3e remains *uninterrupted* for  $x < 0$ .

When draping is included, the ring of high ENA flux disappears from the  $x < 0$  and  $y < 0$  half spaces in Figures 3b and 3d, respectively. In contrast, the ENA images in Figures 3a and 3e share a similar morphology between the uniform and draped cases. The changes introduced in the images taken at  $(0, -3R_C, 0)$  and  $(3R_C, 0, 0)$  can largely be attributed to the asymmetric region of enhanced magnetic field displayed in Figure 4: as found by Haynes et al. (2023), parent protons with pitch angles near  $90^\circ$  are deflected away from the moon by the extended pile-up region. Since this region is largely confined to the upstream portion of the  $y < 0$  half space, proton deflection mainly occurs on Callisto's Jupiter-averted side. Parent protons are therefore unable to reach this portion of Callisto's atmosphere, so they cannot emit ENAs into the detectors located at  $(0, -3R_C, 0)$  and

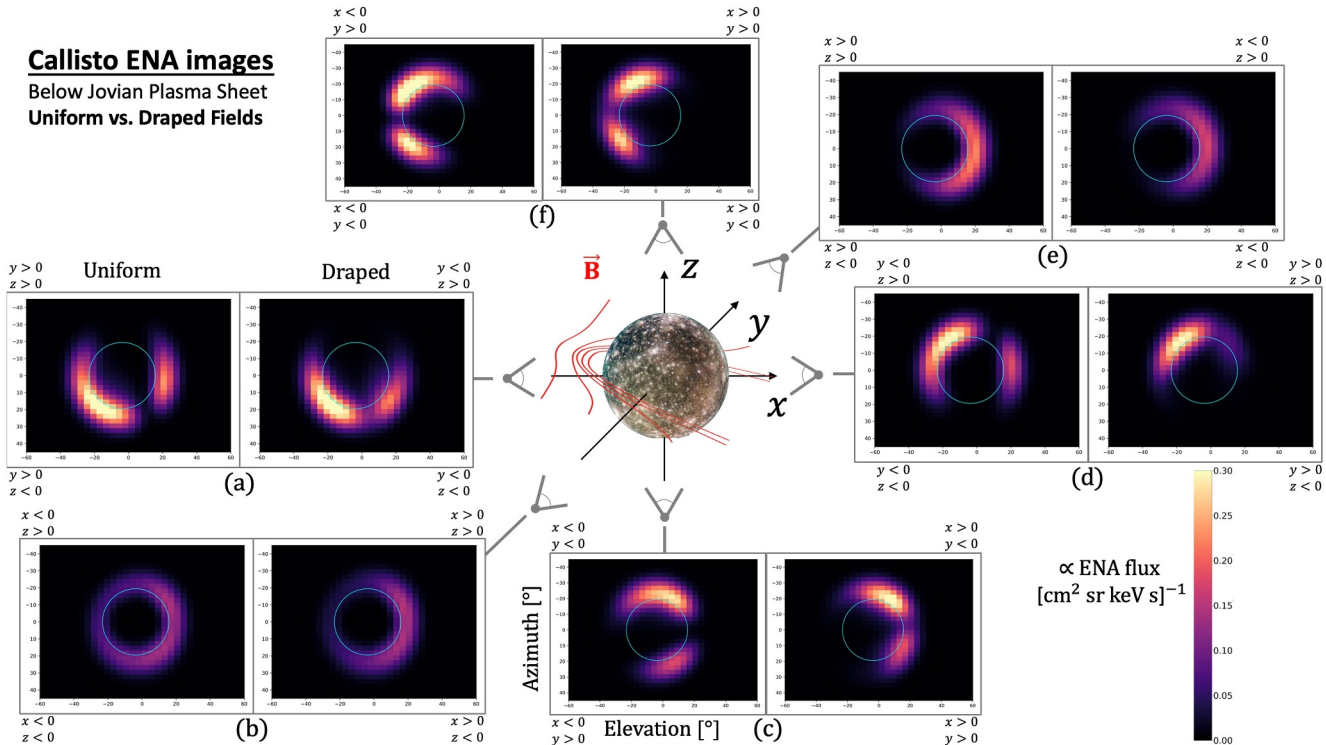


**Figure 6.** Synthetic ENA images of the magnetosphere-atmosphere interaction at Callisto when the moon is at maximum distance below the center of the Jovian plasma sheet. The layout of the figure is analogous to that of Figure 3. In each panel (a)–(f), synthetic ENA images in uniform (left) and draped (right) magnetospheric fields are arranged with detector elevation on the horizontal axis and detector azimuth on the vertical axis. The disc of the moon is represented by the light blue circle in each image. The four corners of each panel are labeled according to the octants of the Satellite Interaction System. The modeled ENA flux for our choice of  $\Delta t$  (see Section 2.2) is indicated by the colorbar in the bottom right-hand corner of the figure, the range of which is 1/60 that of the colorbar in Figure 3. Each panel is connected to a gray detector symbol that illustrates the viewing geometry used to create the respective synthetic ENA images. A sketch of the draped magnetic field lines near Callisto is included in red; the ambient magnetospheric field  $\mathbf{B}_0$  in this configuration forms an angle of only  $10^\circ$  with the  $z = 0$  plane.

$(3R_C, 0, 0)$ . Thus, localized depletions are introduced to the ring of elevated ENA flux on the Jupiter-averted side of the moon by the draped fields in Figures 3b and 3d.

### 3.1.2. Callisto Below the Jovian Plasma Sheet

Figure 6 displays synthetic ENA images for Callisto when the moon is at maximum distance below the center of the Jovian plasma sheet. The figure is arranged in the same way as Figure 3. The ambient magnetic field  $\mathbf{B}_0 = (9.0, 35.3, -6.6)$  nT points mostly in the  $(+y)$  direction. The field lines form an angle of only  $10^\circ$  with Callisto's equatorial plane ( $z = 0$ ). The projections of the field vectors onto the equatorial plane are slightly tilted toward downstream, forming an angle of  $\eta = 14.6^\circ$  with the  $(+y)$  axis. For detectors located at  $(0, -3R_C, 0)$  and  $(0, +3R_C, 0)$ , that is, Figures 6b and 6e, the respective boresight vectors are nearly aligned and anti-aligned with the ambient magnetic field. This is also the case for the detectors in Figures 3c and 3f. For uniform fields, the images in Figure 3 depict a complete ring of elevated ENA flux. In contrast to this, Figure 6e shows a crescent pattern of elevated ENA flux mostly in Callisto's upstream hemisphere, with a gap around the downstream side of the moon. The ring of elevated ENA flux in Figure 6b does not have any gaps, but it is still non-uniform: the lowest flux values occur upstream ( $x < 0$ ) and are shifted slightly northward from the equatorial plane ( $z > 0$ ). Similar to Figure 3, little to no ENA flux is recorded within Callisto's disc at any of the six detector positions.

Even the small tilt  $\eta$  of the magnetic field vectors toward downstream produces a disparity in proton accessibility between lines of sight extended into the  $x < 0$  and  $x > 0$  hemispheres. To illustrate this, Figure 7 shows the geometry of the tilted magnetic field lines in the  $z = 0$  plane. For this example, the detector is positioned at  $(0, +3R_C, 0)$ , corresponding to Figure 6e. In Figure 7a, two lines of sight are extended within this plane into the upstream ( $x < 0$ ) hemisphere: one runs tangent to Callisto's surface, forming an angle of  $\beta_C = \arcsin(1/3) = 19.5^\circ$  with the detector's boresight vector  $(0, -1, 0)$ . The other one is tangential to the

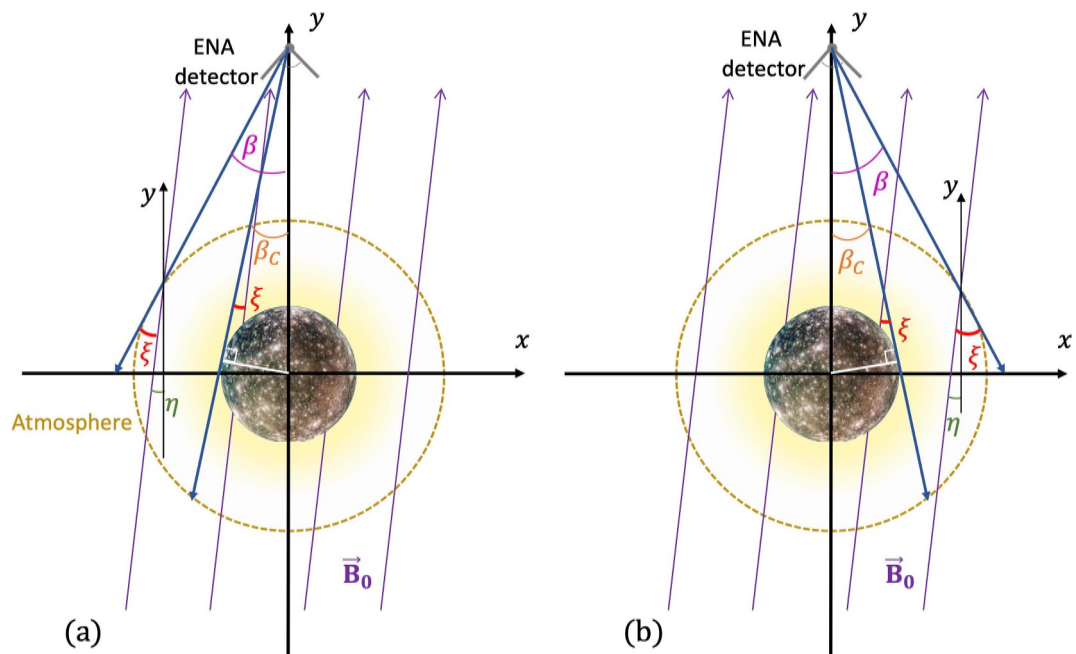


**Figure 7.** Schematic depicting the asymmetric shielding of parent protons by Callisto due to the tilted magnetospheric field  $\mathbf{B}_0$ , shown in the  $z = 0$  plane. For the detector located at  $(0, +3R_C, 0)$ , the range of possible angles  $\xi$  (red) between a LOS and the ambient field  $\mathbf{B}_0$  is compared between the upstream ( $x < 0$ ) and downstream ( $x > 0$ ) hemispheres in panels (a) and (b), respectively. Jovian magnetospheric field lines are displayed in purple, with the tilt angle  $\eta \approx 14.3^\circ$  between  $\mathbf{B}_0$  and the  $(+y)$  axis. The detector is represented by the conjoined gray line segments, with a blue LOS extended toward the innermost and outermost edges of the atmospheric neutral gas outside of Callisto's disc on (a) the upstream side and (b) the downstream side. These lines of sight form angles of  $\beta_C$  (inner edge, orange arc) and  $\beta$  (outer edge, magenta arc) against the boresight vector  $(0, 0, -1)$ , respectively. The dashed yellow circle represents the upper boundary of our model atmosphere.

upper boundary of the model atmosphere at  $|\mathbf{r}| = 2R_C$  and is inclined against the boresight by  $\beta = \arcsin(2/3) = 41.8^\circ$ . In Figure 7b, the two corresponding lines of sight (and associated angles) in the  $x > 0$  hemisphere are shown. These four lines represent the minimum ( $\beta_C$ ) and maximum ( $\beta$ ) deviations from the boresight direction for ENA trajectories detectable outside of Callisto's disc on either side of the moon.

Again neglecting the small  $\mathbf{E}_0 \times \mathbf{B}_0$  drift velocity, the angle  $\xi$  between a LOS and the magnetospheric field lines determines (in uniform fields) the pitch angle  $\alpha$  that a parent proton must have in order to emit an ENA into that pixel on the detector. Using Figure 7a, we can calculate the range of  $\xi$  for lines of sight extended toward the upstream half space ( $x < 0$ ). Since the magnetic field lines are tilted *toward* such a LOS in this half space, the angle  $\xi$  ranges from  $\beta_C - \eta = 4.9^\circ$  to  $\beta - \eta = 27.2^\circ$ . The range of pitch angles for parent protons that can emit ENAs along these lines is identical to the range of  $\xi$ , namely  $\alpha \in \{4.9^\circ, 27.2^\circ\}$ . In contrast, the range of  $\xi$  for a LOS extended toward the downstream ( $x > 0$ ) half space is from  $\beta_C + \eta = 34.1^\circ$  to  $\beta + \eta = 56.4^\circ$ , with the same range for pitch angles given by  $\alpha \in \{34.1^\circ, 56.4^\circ\}$ . In the  $x > 0$  half space, the magnetic field lines are tilted *against* this detector's lines of sight. Therefore, the set of all  $\xi$  values are elevated by  $2\eta$  compared to the  $x < 0$  half space (Figure 7a versus Figure 7b). Thus, in the downstream half space, the pitch angles of protons contributing to the ENA image are closer to  $\alpha = 90^\circ$  than in the upstream half space (where they are closer to  $\alpha = 0^\circ$ ). The gyroradius is proportional to  $\sin \alpha$ . Because of this, parent protons bearing toward a LOS in the  $x > 0$  half space (with near-perpendicular pitch angles and larger gyroradii) are more likely to impact the moon's surface before reaching the LOS than those traveling (with a steeper pitch angle) toward a LOS with the same tilt against the boresight but in the  $x < 0$  half space. In consequence, when the detector is positioned at  $(0, +3R_C, 0)$ , the ENA flux into the ring peaks in the  $x < 0$  half space where the associated parent ions possess the smaller range of gyroradii, whereas a reduction in flux is formed for  $x > 0$  (Figure 6e). When the detector is located at  $(0, -3R_C, 0)$ , a LOS extending into the  $x < 0$  half space makes a *larger* angle  $\xi$  against the magnetic field lines than one with the same tilt against the boresight  $(0, 1, 0)$  in the  $x > 0$  half space. Thus, the ENA flux into the ring is reduced for  $x < 0$ , as seen in Figure 6b. When the fields are uniform, the slight north-south

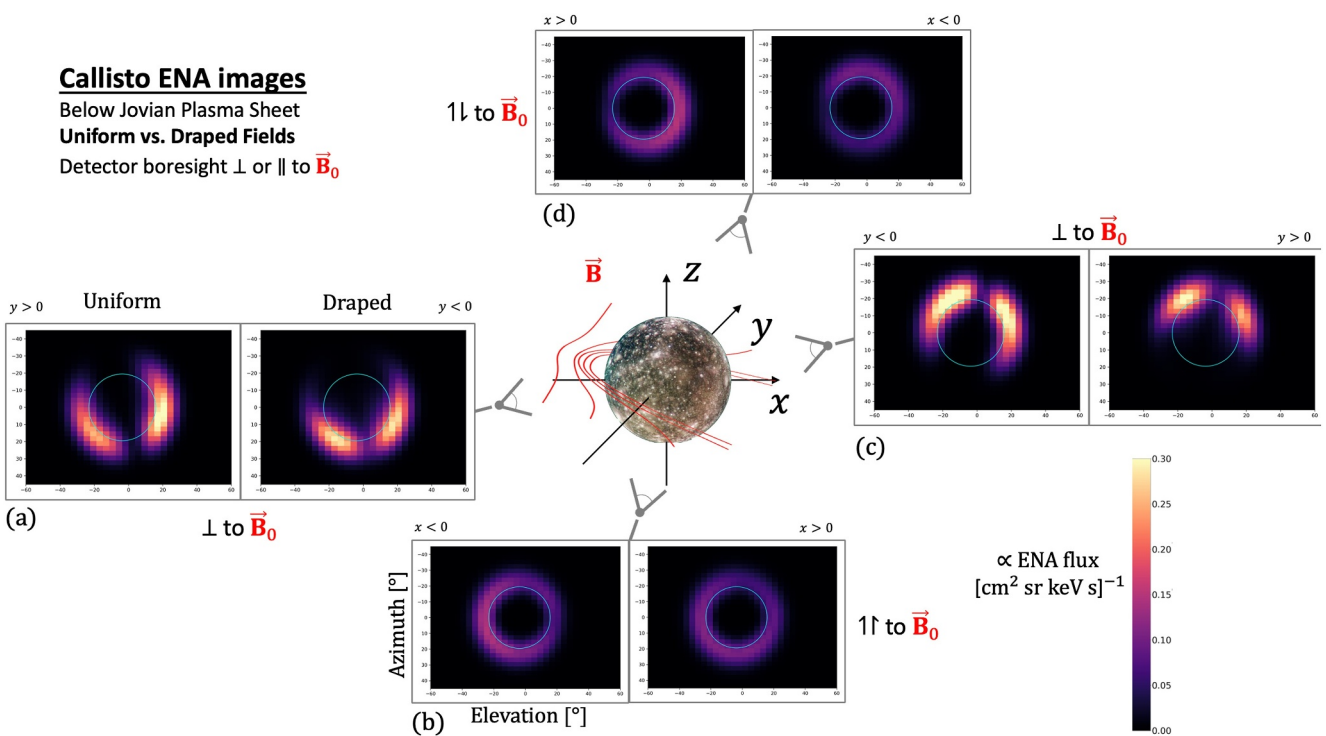


**Figure 8.** Synthetic ENA images at Callisto when the moon is at maximum distance below the center of the Jovian plasma sheet, for boresight vectors aligned with  $\mathbf{B}_0$  (panel (b)), anti-aligned with  $\mathbf{B}_0$  (panel (d)), and perpendicular to  $\mathbf{B}_0$  (panels (a) and (c)). In the counter-clockwise direction (starting with panel (a)), the detector positions read:  $(-1.77, 0, -2.42) R_C$ ,  $(-0.72, -2.86, 0.53) R_C$ ,  $(1.77, 0, 2.42) R_C$ , and  $(0.72, 2.86, -0.53) R_C$ . At all positions, the detector is placed on a sphere of radius  $3R_C$ . For the two boresight orientations perpendicular to the background field, the detector is positioned in the  $y = 0$  plane, upstream of the moon in panel (a) and downstream of it in panel (c). Synthetic ENA images in uniform (left) and draped (right) magnetospheric fields are arranged with detector elevation on the horizontal axis and detector azimuth on the vertical axis. The detectors' azimuth and elevation axes are respectively parallel to the latitude and longitude circles of the West Longitude system which intersect the detector at that point on the sphere. The boresight vector always points toward the center of the moon. The top corners of each panel are labeled to roughly indicate the sectors of the Satellite Interaction System. The modeled ENA flux for our choice of  $\Delta t$  (see Section 2.2) is indicated by the colorbar in the bottom right-hand corner of the figure, with a scale equal to that used for Figure 6. Each panel is attached to a gray detector symbol that approximately shows the viewing geometry used to create the respective synthetic ENA images. The draped magnetic field lines near Callisto are included in red.

asymmetry in the ENA emission pattern of Figure 6b may be caused by the tilt of  $\mathbf{B}_0$  against the  $z = 0$  plane and the nonzero  $\mathbf{E}_0 \times \mathbf{B}_0$  drift.

In order to verify that the non-uniformities of the ENA flux into the rings from Figures 6b and 6e are caused by the tilt between the detector boresight and  $\mathbf{B}_0$ , Figure 8 displays four additional pairs of synthetic ENA images for Callisto located at maximum distance below the center of the Jovian plasma sheet. For all images in Figure 8, the detector is again located on a sphere of radius  $3R_C$  around the moon, with the boresight vector pointing toward its center. The elevation and azimuth axes for these images are parallel to the longitude and latitude circles of the West Longitude system (see, e.g., Section 2 of Haynes et al. (2023)) which run through the detector's position. In these images, the detectors' boresight vectors are oriented parallel to  $\mathbf{B}_0$  (Figure 8b), anti-parallel to  $\mathbf{B}_0$  (Figure 8d), and perpendicular to  $\mathbf{B}_0$  (Figures 8a and 8c). The detectors in Figures 8a and 8c are both located in the  $y = 0$  plane, upstream and downstream of Callisto, respectively.

Due to the small tilt ( $17.5^\circ$ ) of the magnetic field lines against the boresight vector in Figure 6, the viewing geometries in Figures 8b and 8d are only slightly different from those in Figures 6b and 6e. Even still, the morphologies of the respective ENA images are qualitatively different. For the case of a uniform, southward magnetospheric field at the center of the plasma sheet, the two detectors with boresight vectors parallel or anti-parallel to  $\mathbf{B}_0$  record a highly similar ENA emission pattern to that seen in Figure 8 (see Figures 3c and 3f). Thus, regardless of the ambient field orientation, the morphology of the ENA emissions recorded by detectors with boresight vectors precisely parallel or anti-parallel to  $\mathbf{B}_0$  is determined by the density profile of Callisto's atmosphere. When introducing the  $17.5^\circ$  angle between the boresight vector and the magnetic field lines (going from Figures 8b to 6b), the reduction in the ring flips from the upstream to the downstream side. Comparing

Figures 6e and 8d shows the ENA flux is still maximized in the upstream hemisphere, but an extended gap is carved out of the ring on the downstream side. The similarity between the ENA images obtained for the “center” (Figure 3) and “below” (Figure 8) cases with boresight vectors parallel (and anti-parallel) to  $\mathbf{B}_0$  shows that drastic morphological changes are driven by the slight misalignment between the boresight and  $\mathbf{B}_0$ .

In uniform magnetospheric fields, only localized “patches” of high ENA flux occur along the moon’s limb when the boresight vector is contained in the  $y = 0$  plane (Figures 6a, 6c, 6d, and 6f). When the fields are uniform,  $\mathbf{B}_0$  is oriented approximately perpendicular to the detectors’ boresight vectors in these setups. Therefore, the bulk of the ENA flux contributing to these four images is due to parent protons with pitch angles near  $90^\circ$ . When Callisto is at maximum distance below the Jovian plasma sheet, the ambient field is an order of magnitude stronger than at the center of the sheet (see Table 1 of Haynes et al. (2023)). Parent proton gyroradii are reduced by the same factor, so that the scale of gyration in our considered energy range is only about  $(0.1\text{--}0.5)R_C$ . In consequence, only localized regions of Callisto’s atmosphere remain highly accessible to the impinging parent protons (see also Figures 6 and 8 in Liuzzo et al. (2022)). Protons that can still access the atmosphere produce isolated patches of elevated ENA flux near the moon’s limb, as seen in Figures 6a, 6c, 6d, and 6f.

When Callisto is at maximum distance below the Jovian plasma sheet, the induced magnetic dipole moment is near its peak strength (e.g., Hartkorn & Saur, 2017; Zimmer et al., 2000). In order to isolate the contribution of this induction signal to the ENA emission morphology in Figure 6, we have generated a separate series of ENA images for a mere superposition of  $\mathbf{B}_0$  and the induced dipole. This series is discussed in Appendix A. Compared to the case of uniform fields (left images in Figure 6), the induced dipole field imparts only minor modifications to the ENA emission morphology for any of the six viewing geometries considered. The right panels in Figure 6 show synthetic ENA images when the plasma interaction with Callisto’s atmosphere and induced dipole is taken into account. Comparison to the results from Appendix A reveals that the image morphologies obtained for any of the six viewing geometries are very similar to those obtained in the “superposition” scenario. Thus, when Callisto is exposed to the dilute magnetospheric flow far below Jupiter’s plasma sheet, the influence of the field line draping and pile-up on the ENA images is mainly quantitative in nature. The effect of the plasma interaction can be isolated from the contribution of the induced dipole (without plasma currents) only if precise knowledge on the upstream conditions and the 3D atmospheric structure at the time of image acquisition is available. Due to the strong similarities between the ENA images for the superposition setup (right sub-panels in Figure A1) and those including the plasma interaction currents (right panels in Figure 6), the following discussion uses the term “non-uniform fields” to jointly refer to these two scenarios.

Far below the Jovian plasma sheet, non-uniformities in the fields near Callisto introduce appreciable modifications to the ENA image morphology only when the detector is located at  $(+3R_C, 0, 0)$ : the patch of elevated ENA flux around the sub-Jovian ( $y > 0$ ) hemisphere that forms in uniform fields is strongly attenuated, as seen in Figure 6d. While this feature is already weakened in the “superposition” case (Figure A1d), it is removed almost entirely when draping is included in addition (Figure 6d). At the other five detector locations, the changes introduced by non-uniform fields are rather subtle. When the boresight vector is parallel or perpendicular to  $\mathbf{B}_0$  (right images in Figure 8), the synthetic ENA images are again highly similar between uniform and draped fields. For all 10 viewing geometries (Figures 6 and 8), the maximum ENA intensities in the images remain within 15% of their values in uniform fields when draping is included.

The changes brought about by the non-uniform fields stem from the altered accessibility pattern of Callisto’s atmosphere for precipitating parent protons (see Liuzzo et al., 2019b, 2022). The similarity between synthetic ENA images produced for uniform and non-uniform fields in Figures 6 and 8 is consistent with the subtle influence of draping (or the induced dipole in isolation) on the global ENA emission pattern; see Figure 15 of Haynes et al. (2023). Thus, when Callisto is far outside of the Jovian plasma sheet, the presence of any non-uniformities in the fields may be difficult to probe unless the viewing geometry is carefully selected: only for one of our chosen detector locations do such non-uniformities play a significant role in shaping the ENA image (i.e., Figure 6d). At the other detector locations considered, the modifications to the images are likely difficult to discern against the “background” ENA emissions generated by the Jovian magnetosphere (e.g., Mauk et al., 2003).

We do not generate synthetic ENA images for Callisto at maximum distance above the center of the Jovian plasma sheet. In this case, the ambient field orientation and the orientation of the induced dipole are mirrored compared to the “below” case. This will also flip some structures in the synthetic ENA images, but it will not introduce any novel morphological features. The same approach is taken in our study of ENA emissions at Europa. We also note

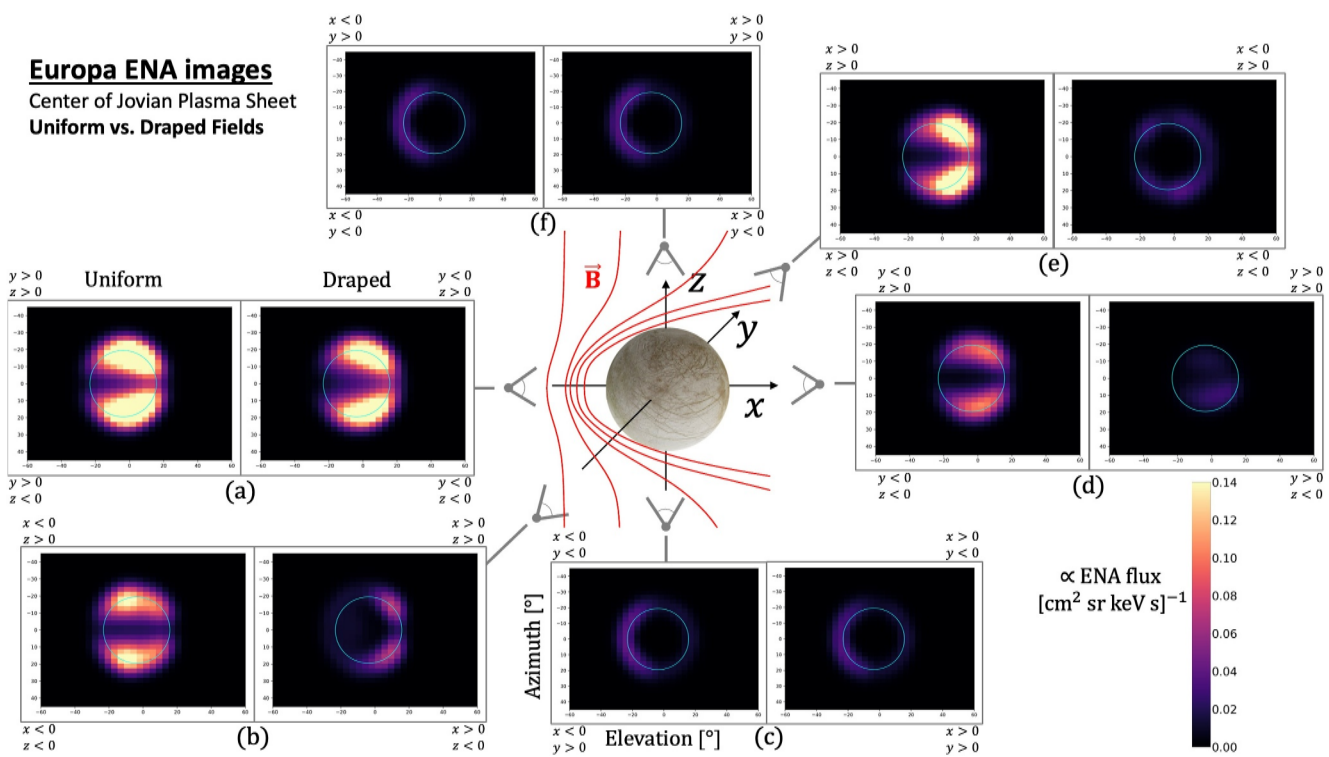


**Figure 9.** Synthetic ENA images of the magnetosphere-atmosphere interaction at Europa when the moon is at the center of the Jovian plasma sheet. The layout of the figure is analogous to that of Figures 3 and 6. In every panel (a)–(f), synthetic ENA images in uniform (left) and draped (right) magnetospheric fields are arranged with detector elevation on the horizontal axis and detector azimuth on the vertical axis. Europa's disc is depicted by the light blue circle in each image. The four corners of each panel are labeled corresponding to the half spaces of the Satellite Interaction System. The colorbar indicates the values of the ENA flux for our choice of  $\Delta t$  (see Section 2.2). Each panel is connected to a gray detector symbol that shows the viewing geometry of the respective synthetic ENA images. A sketch of the draped magnetic field lines near Europa is included in red; the ambient field  $\mathbf{B}_0$  in this configuration is oriented southward, like it is for Callisto in Figure 3.

that using a smaller atmospheric scale height at Callisto (e.g., Liang et al., 2005) would merely shrink the radial extension of the features in the synthetic images.

### 3.2. Analysis of Synthetic ENA Images at Europa

#### 3.2.1. Europa at the Center of the Jovian Plasma Sheet

Figure 9 shows synthetic ENA images at Europa when the moon is at the center of the Jovian plasma sheet. The figure is arranged in an analogous fashion to Figures 3 and 6. For all ENA images in Figure 9, the detector is located at a distance of  $3R_E$  from the origin (i.e., at an altitude of  $2R_E$ ), with a boresight vector directed toward the center of the moon. The ambient magnetospheric field  $\mathbf{B}_0$  points southward in this case. The field magnitude at Europa ( $|\mathbf{B}_0| = 410$  nT) is two orders of magnitude higher than in the “center” case at Callisto. Even for the lowest energy considered, the proton velocity  $\sqrt{2E_0/m_p}$  ( $\approx 979$  km/s) outpaces the  $\mathbf{E}_0 \times \mathbf{B}_0$  drift (100 km/s) by about an order of magnitude.

For the detectors positioned above Europa's poles at  $(0, 0, \pm 3R_E)$ , a ring of elevated ENA flux surrounding the moon's disc is recorded, though extremely faint in the downstream hemisphere (Figures 9c and 9f). For these two images, the boresight vector is aligned or anti-aligned with  $\mathbf{B}_0$ , respectively. Analogous to Callisto (Figures 3c and 3f), parent protons which contribute to the elevated ENA flux in this ring feature must travel through the atmosphere above Europa's limb with velocity vectors nearly parallel or anti-parallel to  $\mathbf{B}_0$ . The ENA flux intensity within the ring peaks at the ramside apex and decreases by a factor of four moving to the downstream hemisphere, where it is approximately constant. In our model, the number density of Europa's atmosphere is maximized above the ramside apex and decreases (in the upstream hemisphere) when moving angularly away from this point toward downstream. The detectors in Figures 9c and 9f capture a side-on view of the atmospheric density profile, and hence, the emissions display a similar morphology. The two detectors located at

( $0, \pm 3R_E, 0$ ) also view the asymmetric neutral profile side-on (Figures 9b and 9e). Thus, the intensity of the ENA emissions in these images decreases when moving from the ramside apex toward downstream ( $x > 0$ ). In contrast, the detectors positioned at ( $\pm 3R_E, 0, 0$ ) do not perceive the ram-wake asymmetry in the atmosphere since the neutral density is rotationally symmetric about the  $x$  axis (Haynes et al., 2023).

The synthetic ENA images taken in Europa's equatorial plane ( $z = 0$ ) display regions of high ENA flux which significantly penetrate into the moon's disc in uniform fields (see Figure 9). For instance, the detector at ( $-3R_E, 0, 0$ ) records the peak in ENA flux *on* Europa's disc. ENA generation largely occurs within one atmospheric scale height (100 km  $\approx 0.07R_E$ ) of the moon's surface (Haynes et al., 2023). Parent protons in our energy range have gyroradii of around 0.02–0.06  $R_E$ , that is, in contrast to Callisto, these are much smaller than the size of the moon. Thus, protons with pitch angles near  $\alpha = 90^\circ$  may readily emit ENAs along a LOS that intersects the atmosphere *between* Europa's surface and the detector at  $2R_E$  altitude, thereby populating the moon's disc with ENA flux. The detectors located above Europa's north and south poles also do not record any ENA flux within the moon's disc (Figures 9c and 9f), akin to the process described for Figures 3c and 3f in Section 3.1.

When the detector is located in the equatorial plane (Figures 9a, 9b, 9d, and 9e), the observed ENA flux in uniform fields is clustered into two “patches” that are symmetric with respect to the equator ( $z = 0$ ). For these viewing geometries, the ambient field  $\mathbf{B}_0$  is normal to the boresight vector. A similarly segmented (but less confined) ENA emission morphology has been revealed at Callisto when *below* the Jovian plasma sheet, again observed by detectors in the plane perpendicular to the magnetic field (Figures 8a and 8c). However, when Callisto is at the *center* of the plasma sheet, detectors with boresight vectors perpendicular to  $\mathbf{B}_0$  see largely uninterrupted rings of elevated ENA flux that encircle the moon's disc (see Figures 3a, 3b, 3d, and 3e). At the center of the sheet, the ambient magnetic field is an order of magnitude weaker than when Callisto is at maximum distance below the plasma sheet.  $|\mathbf{B}_0|$  is increased by another order of magnitude at Europa compared to the Callisto scenario below the plasma sheet. Hence, the segmentation of the ENA emission features near Europa's or Callisto's disc increases with growing ambient field strength (i.e., with decreasing gyroradii  $r_g$ ). In uniform fields, parent protons contributing to the ENA emissions observed by a detector with its boresight perpendicular to  $\mathbf{B}_0$  possess pitch angles near  $90^\circ$ . Thus, for these viewing geometries, the size of the gyroradius (compared to the moon's radius) largely shapes the ENA emission morphology.

In uniform fields, the maximum values of the ENA flux in each image depend strongly on the detector's position. For detectors within the equatorial plane ( $z = 0$ ), the highest ENA fluxes are measured upstream of Europa (Figure 9a), and the peak values drop by about a factor of three moving longitudinally around the moon to its downstream side (Figures 9b, 9d, and 9e). Haynes et al. (2023) found a consistent trend within the band of elevated ENA flux recorded by a spherical detector encompassing Europa's atmosphere. The “global” ENA model also revealed that at a given longitude on the detector sphere, the ENA emissions peak within the equatorial band and fall by a factor of six moving to northern or southern polar latitudes. This decrease in emissions with latitude is similarly consistent with Figure 9: at all four detectors within the equatorial plane (Figures 9a, 9b, 9d, and 9e), the peak ENA flux is approximately 2–6 times greater than that recorded by the detectors above Europa's north and south poles (Figures 9c and 9f). However, we also point out that the global ENA detector does not “filter” the ENA emissions in velocity space in the manner that a realistic ENA imaging instrument does. The conceptual differences between these approaches caution a quantitative comparison between the two model outputs.

When the fields are treated as uniform, the locations of the patches in Figures 9a, 9b, 9d, and 9e are markedly skewed toward one side of the moon's disc, asymmetric with respect to the  $z$  axis and bearing resemblance to “pacman.” For instance, the patches of high ENA flux in Figure 9a are separated in azimuth (vertical axis) by only two pixels at the Jupiter-averted edge of the disc ( $y < 0$ , right side), but by at least 10 at the Jupiter-facing edge ( $y > 0$ , left side). The mechanism driving this dichotomy is illustrated in Figure 10, where we display the four equatorial detectors from Figure 9. The detectors located upstream/downstream are shown in light blue, and the detectors positioned above the sub/anti-Jovian apices are represented in magenta. For each of the detectors, trajectory segments of two protons which contribute to the ENA image depicted in the same color: for example, the two protons in blue could emit ENAs toward both the upstream and downstream detectors.

These trajectory arcs illustrate how a proton's sense of gyration affects the altitudes from which it may emit ENAs into these four detectors. For a southward ambient field  $\mathbf{B}_0$ , the parent protons gyrate counter-clockwise in planes of constant  $z$  when viewed from the north, as depicted by the blue and magenta arcs. When the ENA detector is

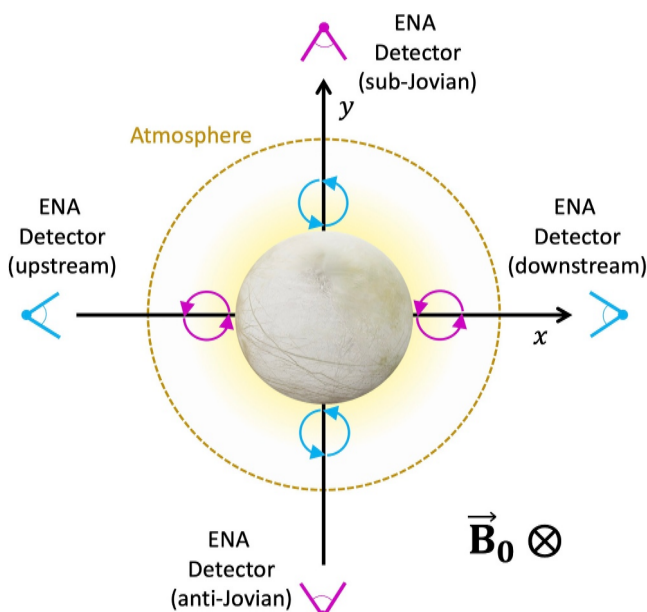


**Figure 10.** Schematic illustrating the gyromotive effect which drives the asymmetric “pac-man” morphology of the ENA emissions recorded by detectors in Europa’s equatorial plane ( $z = 0$ ). The figure depicts a plane of constant  $z$  where  $z \neq 0$ : bright ENA emissions do not occur in the  $z = 0$  plane itself (see Figure 9). For each detector of a given color, the proton gyration arcs in the same color could emit ENAs along a LOS and contribute to the dichotomy in emission morphology seen for that viewing geometry. For instance, the two light blue proton trajectory segments could generate ENA emissions into the detectors located both upstream and downstream of Europa. Note that the gyroradii illustrated here are *not* to scale but are enlarged compared to the size of the moon. The dashed yellow circle represents the upper boundary of Europa’s disc in our model.

positioned upstream (i.e., left blue detector in Figure 10), parent protons can attain a velocity vector parallel to a LOS at lower altitudes on the Jupiter-averted ( $y < 0$ ) side than on the Jupiter-facing side, since those on the Jupiter-facing side bear *away* from the detector when nearest Europa’s surface. In consequence, the patch of elevated ENA flux is more extended in the Jupiter-averted half space than in the Jupiter-facing one (see Figure 9a). This asymmetry in the altitude of ENA production and the associated morphological features flip for the image taken from downstream (right blue detector in Figure 10): as illustrated by the light blue arcs, parent protons can now emit an ENA along a LOS at a lower altitude in the Jupiter-facing half space than in the Jupiter-averted half space, causing the patches of elevated ENA flux to be more pronounced on the  $y > 0$  side of Europa’s disc in Figure 9d.

An analogous dichotomy afflicts the ENA image taken by the detector at  $(0, \pm 3R_E, 0)$ : protons access lines of sight with tangential velocity vectors at lower altitudes in the upstream half space than in the downstream one (see magenta elements of Figure 10). This contributes to the shift of the patches toward upstream for the detector in Figure 9e. According to Figure 10, a similar “pac-man” feature would be expected for the ENA image taken above the anti-Jovian apex, with the patches slightly shifted toward downstream ( $x > 0$ ). However, the equator-facing boundaries of the patches in Figure 9b are nearly parallel to the ( $z = 0$ ) plane. In this case, the visibility of the “pac-man” effect is obscured as a result of two competing processes: (a) the contribution of gyration (Figure 10) tends to shift regions of elevated ENA flux toward downstream; (b) Europa’s atmospheric density is lower in the downstream half space than upstream, thereby counteracting the shift in ENA flux caused by gyration. In contrast to this, when the detector is located above the sub-Jovian apex (Figure 9e), both (a) and (b) tend to enhance the ENA emissions in the upstream half space, making the “pac-man” feature clearly discernible.

When Europa is at the center of the Jovian plasma sheet, field line draping imparts significant modifications to the intensity and/or morphology in three

of the four ENA images taken in the equatorial plane ( $z = 0$ ). When the fields are draped, the images taken from  $(0, \pm 3R_E, 0)$  both exhibit an 85% reduction in flux in the upstream ( $x < 0$ ) half-space, with only a slight (below 20%) weakening in the downstream half space (Figures 9b and 9e). As a result, the peak ENA flux in the right panel of Figure 9b now lies in the downstream half space. The detector positioned downstream at  $(0, 0, 3R_E)$  becomes nearly depleted of ENA flux when draping is included, with the remaining ENA flux observed entirely within the moon’s disc (Figure 9d). In contrast, the detector located upstream of the moon (Figure 9a) still records fluxes in the patches which remain within 20% of their values in uniform fields. The strong modifications to the upstream portions of the ENA images in Figures 9b and 9e are associated with the magnetic field enhancement in Europa’s ramside pile-up region, where the field strength increases to about  $1.6|\vec{B}_0|$  (see, e.g., Figure 3g in Haynes et al. (2023)). For these two detectors, a LOS extended beyond Europa’s limb passes through the upstream atmosphere within the ramside pile-up region, which has a reduced accessibility to protons with pitch angles near  $90^\circ$ . The process of proton deflection by the pile-up region is exemplified in Figure 8 of Haynes et al. (2023). The drastic attenuation of the ENA fluxes seen by the downstream detector (Figure 9d) stems from field line draping, analogous to Callisto (see Section 3.1.1).

When field line draping is incorporated, the ENA flux pattern and intensity observed by the two polar detectors are nearly unaltered from their appearance in uniform fields (Figures 9c and 9f). In contrast to this, field line draping at Callisto qualitatively affects the morphology of the observable ENA emissions for these two viewing geometries (Figures 3c and 3f). The Alfvénic Mach number  $M_A$  at Callisto ( $M_A = 3.45$ ) is substantially larger than at Europa ( $M_A = 0.68$ ; see Table 1 in Haynes et al. (2023)). Therefore, the draped field lines above Callisto’s polar caps are more strongly inclined against the  $z$  axis than at Europa, with the flow-aligned component  $B_x$  reaching  $1.5|\vec{B}_0|$  at Callisto and remaining below  $0.5|\vec{B}_0|$  at Europa (see Figures 3a and 3c in Haynes et al. (2023)). Thus, the draped field lines above Europa’s poles are more aligned with the (straight) background field lines of  $\vec{B}_0$ .

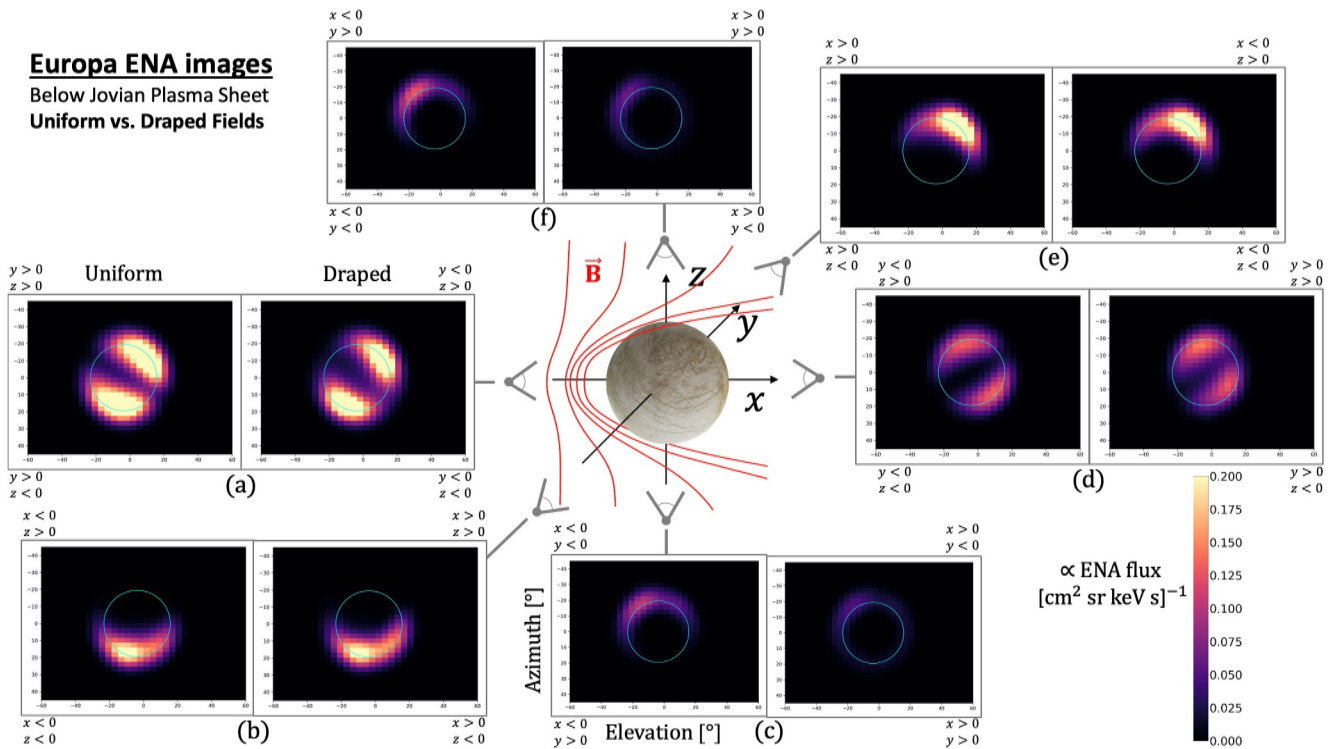


**Figure 11.** Synthetic ENA images at Europa when the moon is at maximum distance below the center of the Jovian plasma sheet. The layout of the figure is analogous to that of Figures 3, 6, and 9, with detector elevation on the horizontal axis and detector azimuth on the vertical axis. Europa's disc is represented by the light blue circle. The four corners of each panel are again labeled according to the sectors of the Satellite Interaction System. The values of the ENA flux for our choice of  $\Delta t$  (see Section 2.2) are represented by the colorbar. A sketch of the draped magnetic field lines near Europa is included in red. The ambient field reads  $\mathbf{B}_0 = (4.0, 209.0, -385.0)$  nT, that is, it is still oriented mainly southward.

than at Callisto, and the trajectories of parent protons with steep pitch angles are less severely impacted at Europa. This explains the weak influence of draping on the ENA images taken above Europa's poles, where the fluxes are altered by no more than 15%.

### 3.2.2. Europa Below the Jovian Plasma Sheet

Figure 11 displays synthetic ENA images in uniform (left sub-panels) and draped fields (right sub-panels) at Europa when the moon is at maximum distance below the Jovian plasma sheet. The figure is arranged in an analogous manner to Figure 9. In this configuration, the ambient magnetospheric field  $\mathbf{B}_0 = (4.0, 209.0, -385.0)$  nT is still oriented mostly southward, making an angle of  $\arctan |B_{y,0}/B_{z,0}| \approx 28.5^\circ$  against the  $(-z)$  axis. The flow-aligned component  $B_{x,0}$  is less than 1% of  $|\mathbf{B}_0|$ , so the magnetic field lines are approximately parallel to the  $x = 0$  plane. The ambient field strength is only about 7% greater than at the center of the plasma sheet. Therefore, parent proton gyroradii are nearly the same in the scenarios from Figures 9 and 11.

When the fields are treated as uniform, the detectors positioned north and south of Europa record elevated ENA flux within a crescent-shaped region around the moon's disc (Figures 11c and 11f). The projection of the ambient field  $\mathbf{B}_0$  onto the  $x = 0$  plane makes an angle of  $\tilde{\eta} = 28.5^\circ$  against the  $(-z)$  axis and is inclined toward Jupiter. Hence, the lines of sight extended into the sub-Jovian and anti-Jovian hemispheres have a different range of inclinations against the magnetic field. This creates a geometric situation analogous to that shown in Figure 7. For the detector located north of Europa (Figure 11f), the geometry from Figure 7a now occurs in the  $y > 0$  half space: the lines of sight which extend toward Europa's limb make a smaller angle against the field lines of  $\mathbf{B}_0$  on the Jupiter-facing side of the moon than on the Jupiter-averted side, thereby driving an elevated ENA flux recorded in the  $y > 0$  portion of the image. A scenario analogous to Figure 7b takes place in the Jupiter-averted ( $y < 0$ ) half space, where the range of angles between the LOS and  $\mathbf{B}_0$  is increased by  $2\tilde{\eta}$ . Therefore, the gyroradii of parent protons in the  $y < 0$  half space are greater than in the  $y > 0$  half space by at least a factor of 3,

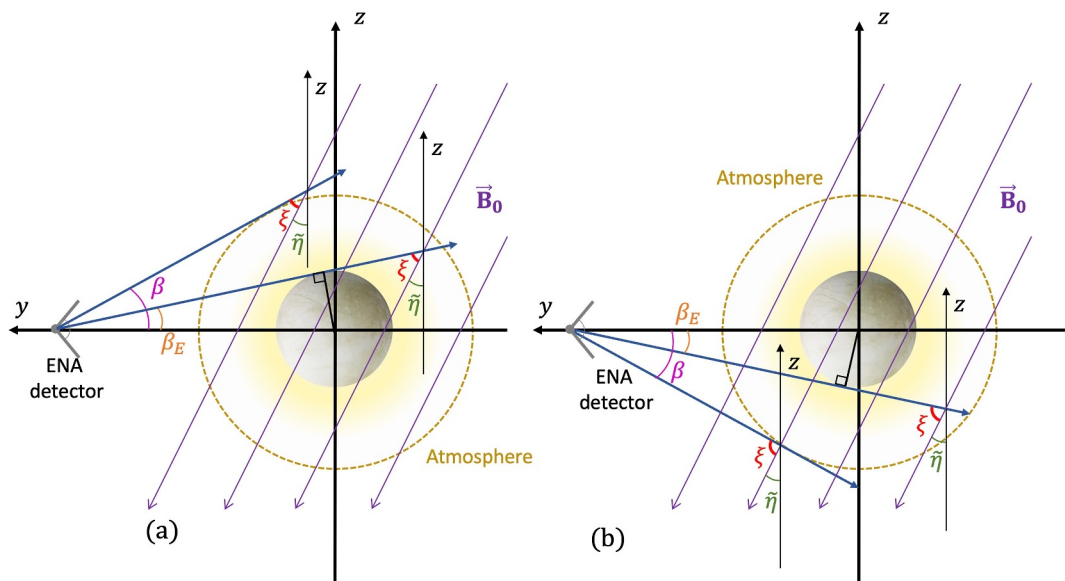


**Figure 12.** Schematic exemplifying the asymmetric range of angles  $\xi$  (red) between  $\mathbf{B}_0$  and a LOS extended from the sub-Jovian detector (Figure 11e) into the northern (panel (a)) and southern (panel (b)) half spaces, shown in the  $x = 0$  plane. Magnetospheric field lines projected into the  $x = 0$  plane are presented in purple, with the tilt angle of  $\tilde{\eta} = 28.5^\circ$  against the  $(-z)$  axis represented in green. The detector is again conveyed by the gray line segments, and the upper boundary of Europa's atmosphere in the model is indicated by the dashed yellow circle. The maximum angle  $\beta$  (magenta) and minimum angle  $\beta_E$  (orange) between the boresight vector and a LOS outside of Europa's disc are also included.

and protons reaching altitudes within one atmospheric scale height are more prone to impacting the surface in the  $y < 0$  hemisphere. Hence, the  $y < 0$  region of the image in Figure 11f is largely devoid of ENA flux. Conversely, when the detector is south of Europa (Figure 11c), the geometry of Figure 7a and thus the “favorable” side for ENA detection can be found in the Jupiter-averted half space. Lines of sight extending into the Jupiter-facing half space make larger angles against the magnetic field. Therefore, the  $y > 0$  region of the image is depleted of ENA flux.

When Europa is at maximum distance below the Jovian plasma sheet, the detectors positioned upstream and downstream of the moon again reveal two patches of elevated ENA flux above the north and south poles, partially populating the moon's disc (Figures 11a and 11d, respectively). In the “pac-man” morphology seen at the center of the plasma sheet, the gap of low flux was aligned with Europa's equator. However, the gap in Figures 9a and 9d is rotated around the boresight vectors  $(\pm 1, 0, 0)$ . For instance, in Figure 11a, the gap forms an angle of  $26^\circ$  against the horizontal ( $0^\circ$  azimuth) axis of the image. This rotation corresponds to the tilt  $\tilde{\eta}$  of the magnetic field lines projected onto the  $x = 0$  plane against the north-south direction, which causes an analogous rotation of the proton gyroplanes against Europa's equator. In consequence, the gap in the “pac-man” feature is rotated against the horizontal axes of the images by approximately the same angle  $\tilde{\eta}$ . When Europa is at maximum distance below Jupiter's plasma sheet, the global ENA model of Haynes et al. (2023) revealed a similar rotation of the band of elevated ENA flux against the moon's equatorial plane: these authors found the tilt of  $\mathbf{B}_0$  to be responsible for the rotation.

In contrast to the images taken at the center of Jupiter's plasma sheet, the detectors positioned at  $(0, \pm 3R_E, 0)$  record only *a single* patch of elevated ENA flux (Figures 11b and 11e). This feature is located in the northern hemisphere for the detector on the sub-Jovian side of Europa (Figure 11e), and in the southern hemisphere for the detector on the anti-Jovian side (Figure 11b). To investigate the processes that may produce the dichotomy between these two ENA images, we calculate the range of pitch angles for parent protons reaching a LOS in either the northern half space (Figure 12a) or southern half space (Figure 12b). As exemplified by Figure 12a, the angle  $\xi$  between the magnetic field lines and a LOS is bounded between  $90^\circ - (\tilde{\eta} + \beta) = 19.7^\circ$  and  $90^\circ - (\tilde{\eta} + \beta_E) = 42.0^\circ$  in the north. Here  $\beta_E$  and  $\beta$  represent the minimum and maximum opening angles (measured against the boresight) for a LOS intersecting Europa's atmosphere outside the moon's disc,

respectively. The range of  $\xi$  values is identical to the range of pitch angles for parent protons that can contribute to the northern half of the ENA image:  $\alpha \in \{19.7^\circ, 42.0^\circ\}$ . Protons with such pitch angles are translating southward, so the gyroplanes are tilted “downward” in the geometry of Figure 12. The range of pitch angles also implies that protons approaching from the south cannot contribute to the northern portion of the ENA image.

In contrast, south of Europa  $\xi$  ranges between  $90^\circ + \beta_E - \tilde{\eta} = 81.0^\circ$  and  $90^\circ + \beta - \tilde{\eta} = 103.3^\circ$ , corresponding to pitch angles of  $\alpha \in \{81.0^\circ, 90.0^\circ\}$  for a proton coming from the north and  $\alpha \in \{90.0^\circ, 103.3^\circ\}$  for a proton coming from the south (Figure 12b). Protons approaching from the north must pass the solid body of Europa before entering the  $z < 0$  half space, making them prone to absorption prior to connecting to a LOS in the south (due to their nonzero gyroradii). In addition, when emitting an ENA in the south, the guiding center of such a proton can be no closer to the surface than  $(1/\cos\tilde{\eta} - 1)R_E \approx 0.14R_E$ . Even for the largest proton gyroradii in our model ( $r_g = 0.06R_E$  at  $E_7 = 75$  keV), these particles travel only through Europa's dilute upper atmosphere. Hence, they make only weak contributions to the ENA flux. Conversely, protons coming from the south can emit ENAs into the detector only below the LOS which is perpendicular to  $\mathbf{B}_0$ . The minimum altitude of this “critical” LOS is  $(3 \sin\tilde{\eta} - 1)R_E \approx 0.43R_E$ . Thus, these protons remain far outside the most dense part of the atmosphere and can contribute only a weak ENA flux. These effects explain the absence of substantial ENA flux in the lower half of the image from Figure 11e. Analogously, for the detector located at  $(0, -3R_E, 0)$ , protons that produce detectable ENAs in the *northern* half space have a reduced atmospheric accessibility compared to the southern half space, thereby contributing to the depletion in ENA flux for  $z > 0$  in Figure 11b.

Similar to Callisto, the induced dipole field at Europa is near its peak strength when the moon is at its maximum distance from the center of the Jovian plasma sheet. We have again generated synthetic ENA images for a mere superposition of  $\mathbf{B}_0$  and the moon's induced dipole, as discussed in Appendix B. Compared to the case of uniform fields, the induction signal imparts minor changes ( $\leq 10\%$ ) to the detectable ENA flux, while leaving the morphology of the synthetic images unaltered. Similar to our findings at Callisto for the corresponding case, the weak field line draping at Europa only slightly adjusts the observable ENA emissions from their appearance with the superposition of the dipole and  $\mathbf{B}_0$  (see also Appendix B). Thus, we discuss both the “superposition” scenario (right panels in Figure B1) and the “plasma interaction” scenario (right panels in Figure 11) in conjunction, again referring to them jointly with the term “non-uniform fields.”

Comparison between the left and right panels in Figures 11 and B1 reveals no distinct morphological differences between the ENA images for uniform and non-uniform fields. The thermal plasma density upstream of Europa falls by about 80% moving from the center to maximum distance below the Jovian plasma sheet (e.g., Roth et al., 2014). In consequence, the magnetic field perturbations generated by the plasma interaction are weakened in magnitude by about a factor of two (compare, e.g., Figures 3g and 3h in Haynes et al. (2023)). Even below the center of the Jovian plasma sheet, the ambient field near Europa still points mainly southward. Therefore, the induced field is weak compared to the magnetospheric field (e.g., Zimmer et al., 2000) and produces only minor perturbations to the observable ENA emissions (see Appendix B). Hence, when Europa is at maximum distance below the Jovian plasma sheet, the influence of any non-uniformities in the moon's electromagnetic environment may be challenging to discern in ENA images.

#### 4. Summary and Concluding Remarks

We have established a model to characterize the morphology of ENA emissions at Europa and Callisto, as observable by a spacecraft detector. Such ENAs are generated through charge exchange interactions between energetic magnetospheric ions and atmospheric neutral gas. Each ENA travels along a tangent line to its parent ion's trajectory at the moment of charge exchange. The dynamics of the energetic parent ions are governed by the electromagnetic fields near each moon. Thus, in contrast to a magnetometer which provides the field vectors only along the spacecraft trajectory, the ENA emissions at both moons are encoded with information about the fields on a global scale. The first ENA camera to chart the morphology of detectable ENA emissions at Europa and Callisto is currently en route to Jupiter aboard the JUICE spacecraft (Galli et al., 2022; Grasset et al., 2013; Tosi et al., 2024).

We employ the AIKEF hybrid model (Müller et al., 2011) to determine the three-dimensional structure of the draped electromagnetic fields near Europa and Callisto. These fields are then incorporated into a tracing tool for the energetic parent ions to calculate synthetic ENA images. For the synthetic ENA images generated in this

paper, this tool launches energetic parent protons along the detector's lines of sight and traces them backwards in time. The ENA flux emitted by these protons into every detector pixel is subsequently assembled into a synthetic ENA image, in a similar fashion to a mosaic.

To emulate image acquisition by an actual ENA detector, we consider a (hypothetical) energy channel spanning from  $E = 5$  keV to  $E = 75$  keV. In order to study the ENA emission morphology from multiple vantages, we position detectors with boresight vectors oriented parallel/anti-parallel and perpendicular to the ambient magnetospheric field  $\mathbf{B}_0$ , as well as inclined against it. In all our synthetic ENA images, the detector's boresight vector points radially inward toward the center of the moon, that is, it is contained in a plane through the center. Each detector is placed outside of the atmosphere at an altitude of two moon radii from the surface. We generate sets of ENA images for Europa and Callisto located at the center and at maximum distance below the Jovian plasma sheet. In this way, we assess the variability of ENA observations. For each of these two configurations, we produce synthetic ENA images for both uniform and draped fields, revealing the influence of non-uniformities in Europa's and Callisto's electromagnetic environments on the detectable ENA emissions. To isolate the impact of the induced field from each moon's subsurface ocean and/or ionosphere on the ENA images, we carry out additional runs using a mere superposition of the ambient magnetospheric field  $\mathbf{B}_0$  with the induced dipole. We report our major findings as follows:

- Charge exchange between energetic magnetospheric protons and atmospheric neutrals produces distinct ENA emissions at Europa and Callisto that may be detected by a spacecraft outside each moon's atmosphere. In (hypothetically) uniform electromagnetic fields, the observable ENA flux populates segments of a ring along Europa's or Callisto's disc. The radial and angular extents of these segments depend on the orientation of the detector's boresight vector with respect to the background field  $\mathbf{B}_0$  as well as the ambient field strength  $|\mathbf{B}_0|$  which determines the gyroradii of the parent protons.
- When the detector's boresight is perpendicular to the ambient field  $\mathbf{B}_0$ , the fragmentation of the ENA emission features into distinct segments of elevated flux grows with ambient field magnitude. This increased fragmentation is caused by the reduction of the parent proton gyroradii with respect to the size of the moon as  $|\mathbf{B}_0|$  gets stronger. Locations within the ring where the ENA flux is enhanced are determined by the parent protons' sense of gyration and the direction of their  $\mathbf{E}_0 \times \mathbf{B}_0$  drift.
- In uniform fields, parent protons with steep pitch angles generate a ring of elevated ENA flux around Europa's or Callisto's disc. The uninterrupted ring is observable by detectors that have boresight vectors aligned or anti-aligned with  $\mathbf{B}_0$ . Absorption by Europa's or Callisto's solid body depletes the disc itself of observable ENA flux.
- When the detector boresight is neither parallel/anti-parallel nor perpendicular to the ambient field  $\mathbf{B}_0$ , parent protons contributing to segments of elevated ENA flux in the image have different gyroradii on either side of the moon. Absorption of a fraction of these protons at the surface results in a reduced ENA flux on the side where larger gyroradii are required, yielding a hemispheric asymmetry in the intensity of detectable ENA flux.
- When Europa or Callisto are near the center of the Jovian plasma sheet, the interaction with the impinging flow generates the strongest field perturbations and is most effective at deflecting energetic proton trajectories (see also Haynes et al., 2023). However, draping is visible in the ENA images only for certain viewing geometries. For instance, when Callisto is at the center of the sheet, the asymmetry in the magnetic pile-up region cuts away a segment of elevated flux in ENA images taken from above the moon's geographic poles. When either moon is at maximum distance below the Jovian plasma sheet, non-uniformities in the fields are generated by both the plasma interaction and the induction signal. However, these non-uniform fields leave the morphology of the features in the ENA images largely unchanged and have only a minor, quantitative impact on the intensity of the observed emissions. Thus, for the upcoming JUICE encounters of Europa and Callisto, the viewing geometry must be carefully selected to observe signatures of the plasma interaction or any induced fields with ENA imaging.
- Asymmetries in the atmospheric neutral density are discernible in ENA images at both moons. Such asymmetries are predicted by models of Europa's and Callisto's neutral envelopes (e.g., Addison et al., 2021; Carberry Mogan et al., 2023; Oza et al., 2019). Hence, ENA imaging has the potential to remotely characterize atmospheric asymmetries at both moons on a global scale.
- At both moons, the induced magnetic field from the subsurface ocean and/or ionosphere makes only subtle, quantitative contributions to the ENA emission morphology.

In the future, the model presented here can be applied to support the planning and analysis of ENA observations along scheduled JUICE flybys of Callisto and Europa. In particular, our approach allows us to compare the morphology of ENA emissions from the magnetosphere-atmosphere interactions at both moons to the emission pattern of ENAs released from their surfaces (see also Pontoni et al., 2022; Szabo et al., 2024). However, the current version of the model provides information only on the morphology, but not the absolute intensities of the features in the ENA images. This will change as soon as initial observations of the ENA emissions at Europa and Callisto become available to calibrate the model.

## Appendix A: Influence of Callisto's Induced Dipole on the Morphology of Synthetic ENA Images

Figure A1 shows synthetic ENA images for Callisto at maximum distance below the center of the Jovian plasma sheet. The layout of the figure is the same as in Figure 6. These images are calculated with uniform electromagnetic fields (left plots) and compared to those calculated for a superposition of the background field  $\mathbf{B}_0$  with the induced dipole (right plots). This setup represents an “intermediate case” between uniform and draped fields, since no plasma interaction currents are included. Therefore, comparison between the left and right panels in Figure A1 allows the isolation of modifications to the ENA images caused by Callisto’s induced dipole field specifically. In addition, comparison to the images for draped fields in Figure 6 reveals changes introduced by the plasma interaction.

The differences between ENA images with uniform fields and the induced dipole field are largely *not* morphological, but quantitative in nature. The induced dipole modifies the magnetospheric field near Callisto by more than 50% only in isolated regions just above the surface (e.g., Liuzzo et al., 2015). In consequence, adding the dipole field to  $\mathbf{B}_0$  has a largely minor impact on the accessibility of the moon’s atmosphere to energetic parent protons (Liuzzo et al., 2019b). Only in Figure A1d, the “patch” of elevated ENA flux visible in the  $y > 0$  half

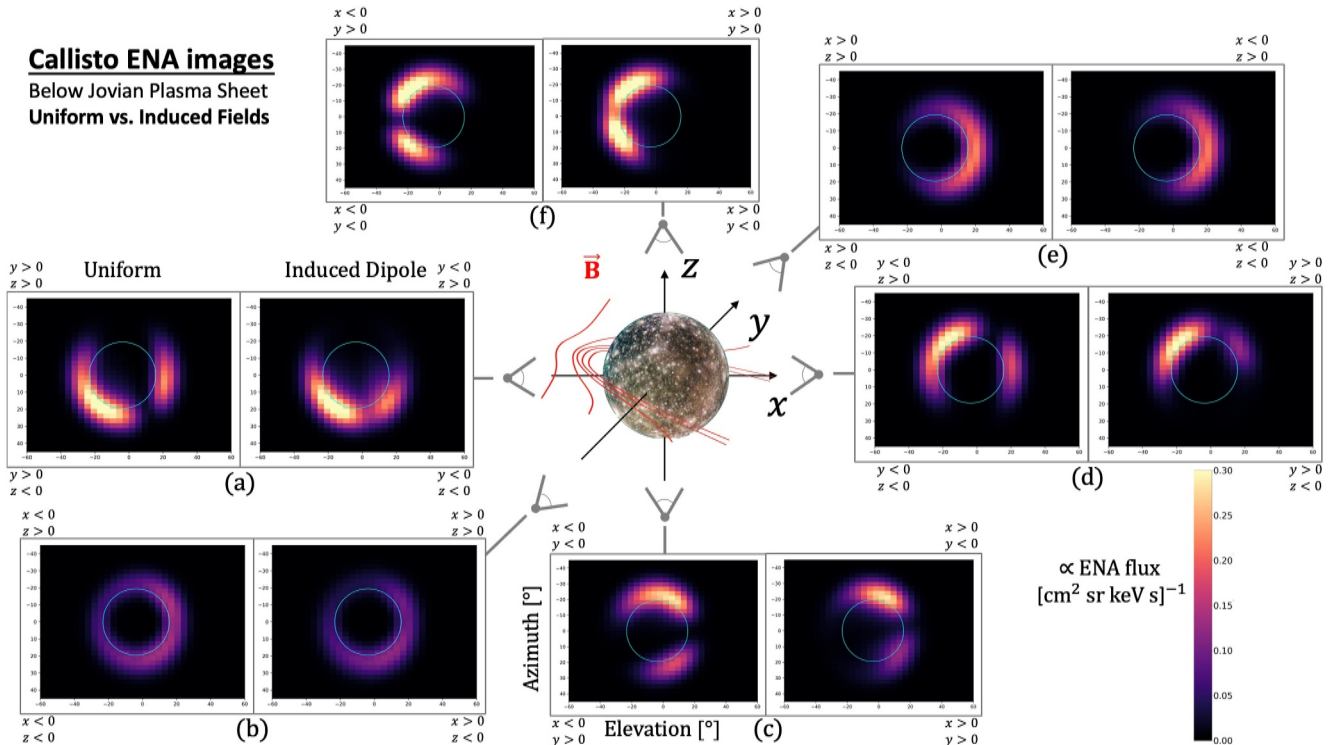


**Figure A1.** Synthetic ENA images illustrating the effect of the induced dipole when Callisto is at maximum distance below the center of the Jovian plasma sheet. The layout of the figure is the same as that of Figure 6. The ENA images on the left side of each panel are for uniform fields (i.e., these are identical to the left images in Figure 6), and the right images are calculated using the superposition of the ambient magnetospheric field  $\mathbf{B}_0$  and the induced dipole field. At Callisto, the induced dipole moment for this configuration is given by  $\mathbf{M}_{\text{ind}} = (-0.63, -2.50, 0) \cdot 10^{27}$  J/nT. None of the images shown here include contributions from plasma currents to parent proton trajectories. The detector is positioned at  $|\mathbf{r}| = 3R_C$ , and the boresight vector always bears toward the center of the moon.

space for uniform fields is strongly diminished in extension and magnitude when Callisto's induced dipole field is included. The global model of Haynes et al. (2023) revealed that Callisto's induced dipole redistributes a small portion of the ENA flux produced by parent protons with pitch angles near  $90^\circ$ . This effect contributes to the differences between the left and right ENA images in Figure A1d.

## Appendix B: Influence of Europa's Induced Dipole on the Morphology of Synthetic ENA Images

Figure B1 displays synthetic ENA images for Europa at maximum distance below the center of the Jovian plasma sheet. Images in the left sub-panels are calculated with the ambient magnetospheric field  $\mathbf{B}_0$  and electric field  $\mathbf{E}_0 = -\mathbf{u}_0 \times \mathbf{B}_0$ , that is, they are identical to the left images in Figure 11. Images in the right sub-panels are calculated using a superposition of  $\mathbf{B}_0$  and Europa's induced dipole field. Similar to our findings at Callisto, the induced dipole at Europa imparts minor quantitative changes on the synthetic ENA images, but leaves the morphology of the emission patterns largely unchanged. For detectors above the moon's north and south poles, the peak intensity of the ENA emissions is reduced by nearly a factor of two with the inclusion of the induced dipole field (Figures B1c and B1f). However, this reduction is confined to only a few pixels in each image. For the detectors in Europa's equatorial plane ( $z = 0$ ), the peak intensity of the ENA flux is modified by 10% or less when the inductive response is included. Because the magnetospheric field  $\mathbf{B}_0$  is predominantly southward at Europa's orbit, the induced dipole adjusts the field near the moon by no more than  $|\mathbf{B}_0|/5$  (see, e.g., Figures 7 and 9 in Addison et al. (2023)). Therefore, proton trajectories accessing Europa's atmosphere deviate only slightly from their paths through uniform fields, explaining the similarity between the right and left images of each panel in Figure B1.

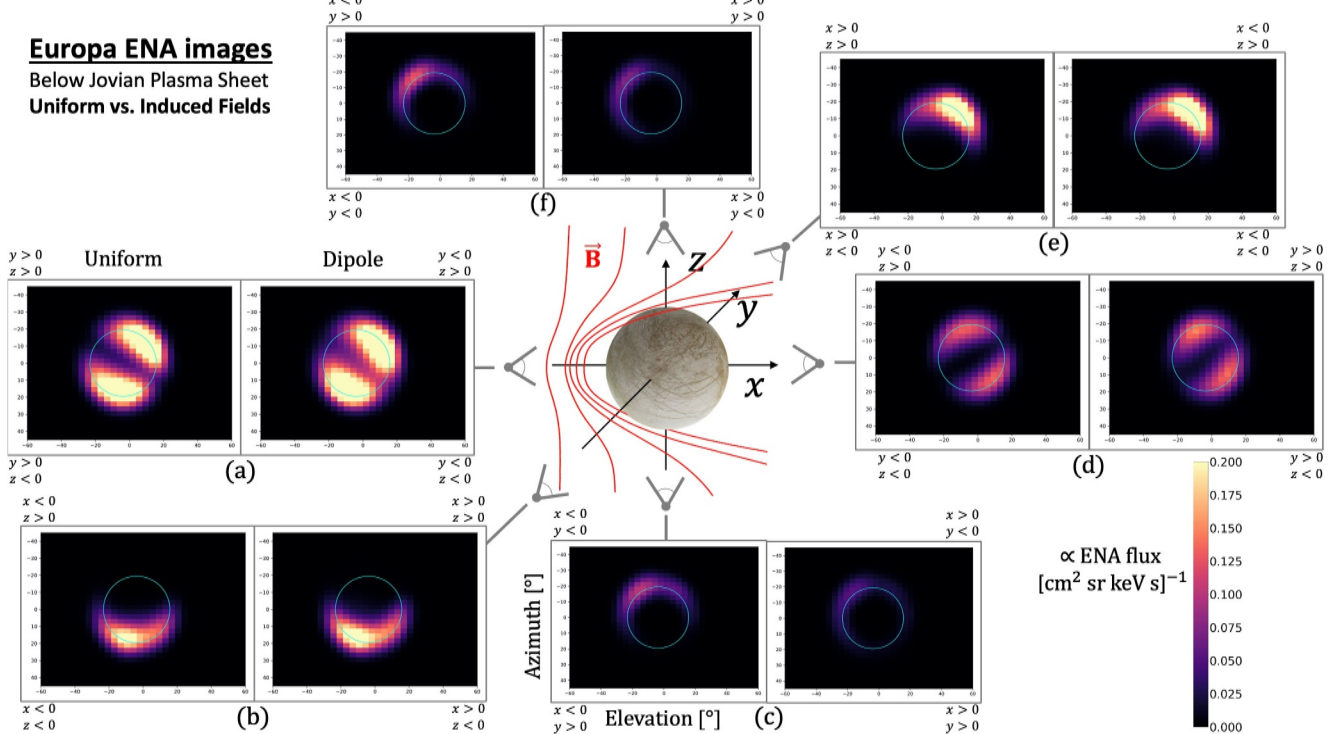


**Figure B1.** Synthetic ENA images depicting the influence of the induced dipole when Europa is at maximum distance below the center of the Jovian plasma sheet. The layout of the figure is identical to that of Figure A1. The ENA images on the left side of each panel are for uniform fields; that is, these are identical to the left images in Figure 11. The right-side images are calculated using a mere superposition of the ambient magnetospheric field  $\mathbf{B}_0$  and the induced dipole field. The induced dipole moment in this configuration reads  $\mathbf{M}_{\text{ind}} = (-0.01, -3.97, 0) \cdot 10^{27}$  J/nT. None of the images shown in this figure include contributions from plasma currents to the trajectories of parent protons.

## Data Availability Statement

Data supporting the production and conclusions of this work can be obtained from Haynes et al. (2024).

### Acknowledgments

The authors acknowledge financial support through NASA's *Solar System Workings Program 2019*, Grant 80NSSC21K0152 as well as *Solar System Workings Program 2020*, Grants 80NSSC22K0097 and 80NSSC23K0351. This body of work was not written or contributed to in any part by an artificial intelligence engine such as GPT. The authors would like to thank Peter Kollmann (Johns Hopkins University, Applied Physics Laboratory) for careful inspection of the manuscript and for valuable comments.

### References

- Addison, P., Haynes, C. M., Stahl, A. M., Liuzzo, L., & Simon, S. (2024). Magnetic signatures of the interaction between Europa and Jupiter's magnetosphere during the Juno flyby. *Geophysical Research Letters*, 51(2), e2023GL106810. <https://doi.org/10.1029/2023GL106810>
- Addison, P., Liuzzo, L., Arnold, H., & Simon, S. (2021). Influence of Europa's time-varying electromagnetic environment on magnetospheric ion precipitation and surface weathering. *Journal of Geophysical Research: Space Physics*, 126(5), e2020JA029087. <https://doi.org/10.1029/2020JA029087>
- Addison, P., Liuzzo, L., & Simon, S. (2022). Effect of the magnetospheric plasma interaction and solar illumination on ion sputtering of Europa's surface ice. *Journal of Geophysical Research: Space Physics*, 127(2), e2021JA030136. <https://doi.org/10.1029/2021JA030136>
- Addison, P., Liuzzo, L., & Simon, S. (2023). Surface-plasma interactions at Europa in draped magnetospheric fields: The contribution of energetic electrons to energy deposition and sputtering. *Journal of Geophysical Research: Space Physics*, 128(8), e2023JA031734. <https://doi.org/10.1029/2023JA031734>
- Arnold, H., Liuzzo, L., & Simon, S. (2019). Magnetic signatures of a plume at Europa during the Galileo E26 flyby. *Geophysical Research Letters*, 46(3), 1149–1157. <https://doi.org/10.1029/2018GL081544>
- Arnold, H., Liuzzo, L., & Simon, S. (2020). Plasma interaction signatures of plumes at Europa. *Journal of Geophysical Research: Space Physics*, 125(1), e2019JA027346. <https://doi.org/10.1029/2019JA027346>
- Arnold, H., Simon, S., & Liuzzo, L. (2020). Applying ion energy spectrograms to search for plumes at Europa. *Journal of Geophysical Research: Space Physics*, 125(9), e2020JA028376. <https://doi.org/10.1029/2020JA028376>
- Bagenal, F., & Delamere, P. A. (2011). Flow of mass and energy in the magnetospheres of Jupiter and Saturn. *Journal of Geophysical Research*, 116(A5), A05209. <https://doi.org/10.1029/2010JA016294>
- Bagenal, F., Sidrow, E., Wilson, R. J., Cassidy, T. A., Dols, V., Crary, F. J., et al. (2015). Plasma conditions at Europa's orbit. *Icarus*, 261, 1–13. <https://doi.org/10.1016/j.icarus.2015.07.036>
- Bagenal, F., Wilson, R. J., Siler, S., Paterson, W. R., & Kurth, W. S. (2016). Survey of Galileo plasma observations in Jupiter's plasma sheet. *Journal of Geophysical Research: Planets*, 121(5), 871–894. <https://doi.org/10.1002/2016JE005009>
- Bhattacharya, D., Clarke, J. T., Montgomery, J., Bonfond, B., Gérard, J.-C., & Grodent, D. (2018). Evidence for auroral emissions from Callisto's footprint in HST UV images. *Journal of Geophysical Research: Space Physics*, 123(1), 364–373. <https://doi.org/10.1002/2017JA024791>
- Bonfond, B., Saur, J., Grodent, D., Badman, S. V., Bisikalo, D., Shematovich, V., et al. (2017). The tails of the satellite auroral footprints at Jupiter. *Journal of Geophysical Research: Space Physics*, 122(8), 7985–7996. <https://doi.org/10.1002/2017JA024370>
- Brandt, P., Dialynas, K., Dandouras, I., Mitchell, D., Garnier, P., & Krimigis, S. (2012). The distribution of Titan's high-altitude (out to 50,000km) exosphere from energetic neutral atom (ENA) measurements by Cassini/INCA. *Planetary and Space Science*, 60(1), 107–114. <https://doi.org/10.1016/j.pss.2011.04.014>
- Breer, B. R., Liuzzo, L., Arnold, H., Andersson, P. N., & Simon, S. (2019). Energetic ion dynamics in the perturbed electromagnetic fields near Europa. *Journal of Geophysical Research: Space Physics*, 124(9), 7592–7613. <https://doi.org/10.1029/2019JA027147>
- Carberry Morgan, S. R., Liuzzo, L., Poppe, A. R., Simon, S., Szalay, J. R., Tucker, O. J., & Johnson, R. E. (2023). Callisto's atmosphere: The oxygen enigma. *Journal of Geophysical Research: Planets*, 128(9), e2023JE007894. <https://doi.org/10.1029/2023JE007894>
- Carberry Morgan, S. R., Tucker, O. J., Johnson, R. E., Roth, L., Alday, J., Vorburger, A., et al. (2022). Callisto's atmosphere: First evidence for H<sub>2</sub> and constraints on H<sub>2</sub>O. *Journal of Geophysical Research: Planets*, 127(11), e2022JE007294. <https://doi.org/10.1029/2022JE007294>
- Carlson, R. (1999). A tenuous carbon dioxide atmosphere on Jupiter's moon Callisto. *Science*, 283(5403), 820–821. <https://doi.org/10.1126/science.283.5403.820>
- Carlson, R., Smythe, W., Baines, K., Barbinis, E., Becker, K., Burns, R., et al. (1996). Near-infrared spectroscopy and spectral mapping of Jupiter and the Galilean satellites: Results from Galileo's initial orbit. *Science*, 274(5286), 385–388. <https://doi.org/10.1126/science.274.5286.385>
- Cervantes, S., & Saur, J. (2022). Constraining Europa's subsolar atmosphere with a joint analysis of HST spectral images and Galileo magnetic field data. *Journal of Geophysical Research: Space Physics*, 127(9), e2022JA030472. <https://doi.org/10.1029/2022JA030472>
- Clark, G., Mauk, B., Paranicas, C., Haggerty, D. K., Kollmann, P., Rymer, A. M., et al. (2019). Energetic particle observations in Jupiter's polar magnetosphere: New discoveries by Juno. In *AGU fall meeting abstracts* (Vol. 2019, p. P42A-01).
- Clark, G., Mauk, B. H., Kollmann, P., Paranicas, C., Bagenal, F., Allen, R. C., et al. (2020). Heavy ion charge states in Jupiter's polar magnetosphere inferred from auroral megavolt electric potentials. *Journal of Geophysical Research: Space Physics*, 125(9), e2020JA028052. <https://doi.org/10.1029/2020JA028052>
- Cohen, C. M. S., Stone, E. C., & Selesnick, R. S. (2001). Energetic ion observations in the middle Jovian magnetosphere. *Journal of Geophysical Research*, 106(A12), 29871–29881. <https://doi.org/10.1029/2001JA000008>
- Connerney, J. E. P., Kotsiaros, S., Oliversen, R. J., Espley, J. R., Joergensen, J. L., Joergensen, P. S., et al. (2018). A new model of Jupiter's magnetic field from Juno's first nine orbits. *Geophysical Research Letters*, 45(6), 2590–2596. <https://doi.org/10.1002/2018GL077312>
- Connerney, J. E. P., Timmins, S., Herceg, M., & Joergensen, J. L. (2020). A Jovian magnetodisc model for the Juno era. *Journal of Geophysical Research: Space Physics*, 125(10), e2020JA028138. <https://doi.org/10.1029/2020JA028138>
- Connerney, J. E. P., Timmins, S., Oliversen, R. J., Espley, J. R., Joergensen, J. L., Kotsiaros, S., et al. (2022). A new model of Jupiter's magnetic field at the completion of Juno's prime mission. *Journal of Geophysical Research: Planets*, 127(2), e2021JE007055. <https://doi.org/10.1029/2021JE007055>
- Cunningham, N. J., Spencer, J. R., Feldman, P. D., Strobel, D. F., France, K., & Osterman, S. N. (2015). Detection of Callisto's oxygen atmosphere with the hubble Space Telescope. *Icarus*, 254, 178–189. <https://doi.org/10.1016/j.icarus.2015.03.021>
- Dandouras, J., & Amsif, A. (1999). Production and imaging of energetic neutral atoms from Titan's exosphere: A 3-D model. *Planetary and Space Science*, 47(10), 1355–1369. [https://doi.org/10.1016/S0032-0633\(99\)00057-4](https://doi.org/10.1016/S0032-0633(99)00057-4)
- de Kleer, K., Milby, Z., Schmidt, C., Camarca, M., & Brown, M. E. (2023). The optical aurorae of Europa, Ganymede, and Callisto. *The Planetary Science Journal*, 4(2), 37. <https://doi.org/10.3847/PSJ/acb53c>
- Dialynas, K., Krimigis, S. M., Mitchell, D. G., Roelof, E. C., & Decker, R. B. (2013). A three-coordinate system (ecliptic, galactic, ISMF) spectral analysis of heliospheric ena emissions using cassini/inca measurements. *The Astrophysical Journal*, 778(1), 40. <https://doi.org/10.1088/0004-637X/778/1/40>

- Galli, A., Vorburger, A., Carberry Mogan, S. R., Roussos, E., Stenberg Wieser, G., Wurz, P., et al. (2022). Callisto's atmosphere and its space environment: Prospects for the particle environment package on board JUICE. *Earth and Space Science*, 9(5), e2021EA002172. <https://doi.org/10.1029/2021EA002172>
- Galli, A., Vorburger, A., Wurz, P., Pommerol, A., Cerubini, R., Jost, B., et al. (2018). 0.2 to 10 keV electrons interacting with water ice: Radiolysis, sputtering, and sublimation. *Planetary and Space Science*, 155, 91–98. <https://doi.org/10.1016/j.pss.2017.11.016>
- Grasset, O., Dougherty, M., Coustenis, A., Bunce, E., Erd, C., Titov, D., et al. (2013). JUpiter ICY moons Explorer (JUICE): An ESA mission to orbit Ganymede and to characterise the Jupiter system. *Planetary and Space Science*, 78, 1–21. <https://doi.org/10.1016/j.pss.2012.12.002>
- Gurnett, D. A., Persoon, A. M., Kurth, W. S., Roux, A., & Bolton, S. J. (2000). Plasma densities in the vicinity of Callisto from Galileo plasma wave observations. *Geophysical Research Letters*, 27(13), 1867–1870. <https://doi.org/10.1029/2000GL003751>
- Hall, D. T., Feldman, P. D., McGrath, M. A., & Strobel, D. F. (1998). The far-ultraviolet oxygen airglow of Europa and Ganymede. *The Astrophysical Journal*, 499(1), 475–481. <https://doi.org/10.1086/305604>
- Hall, D. T., Strobel, D. F., Feldman, P. D., McGrath, M. A., & Weaver, H. A. (1995). Detection of an oxygen atmosphere on Jupiter's moon Europa. *Nature*, 373(6516), 677–679. <https://doi.org/10.1038/373677a0>
- Harris, C. D. K., Jia, X., Slavin, J. A., Toth, G., Huang, Z., & Rubin, M. (2021). Multi-fluid MHD simulations of Europa's plasma interaction under different magnetospheric conditions. *Journal of Geophysical Research: Space Physics*, 126(5), e2020JA028888. <https://doi.org/10.1029/2020JA028888>
- Hartkorn, O., & Saur, J. (2017). Induction signals from Callisto's ionosphere and their implications on a possible subsurface ocean. *Journal of Geophysical Research: Space Physics*, 122(11), 11677–11697. <https://doi.org/10.1002/2017JA024269>
- Haynes, C. M., Tippens, T., Addison, P., Liuzzo, L., Poppe, A. R., & Simon, S. (2023). Emission of energetic neutral atoms from the magnetosphere-atmosphere interactions at Callisto and Europa. *Journal of Geophysical Research: Space Physics*, 128(10), e2023JA031931. <https://doi.org/10.1029/2023JA031931>
- Haynes, C. M., Tippens, T., Simon, S., & Liuzzo, L. (2024). Data for "Constraints on the Observability of Energetic Neutral Atoms from the Magnetosphere-Atmosphere Interactions at Callisto and Europa" by Haynes et al., 2024 [Dataset]. *Zenodo*. <https://doi.org/10.5281/zenodo.1384045>
- Huybrighs, H. L. F., Blöcker, A., Roussos, E., van Buchem, C., Futaana, Y., Holmberg, M. K. G., et al. (2023). Europa's perturbed fields and induced dipole affect energetic proton depletions during distant Alfvén wing flybys. *Journal of Geophysical Research: Space Physics*, 128(9), e2023JA031420. <https://doi.org/10.1029/2023JA031420>
- Kabanovic, S., Feyerabend, M., Simon, S., Meeks, Z., & Wuilms, V. (2018). Influence of asymmetries in the magnetic draping pattern at Titan on the emission of energetic neutral atoms. *Planetary and Space Science*, 152, 142–164. <https://doi.org/10.1016/j.pss.2017.12.017>
- Khurana, K. K. (1997). Euler potential models of Jupiter's magnetospheric field. *Journal of Geophysical Research*, 102(A6), 11295–11306. <https://doi.org/10.1029/97JA00563>
- Khurana, K. K., Kivelson, M. G., Stevenson, D. J., Schubert, G., Russell, C. T., Walker, R. J., & Polanskey, C. (1998). Induced magnetic fields as evidence for subsurface oceans in Europa and Callisto. *Nature*, 395(6704), 777–780. <https://doi.org/10.1038/27394>
- Khurana, K. K., Mitchell, D. G., Arridge, C. S., Dougherty, M. K., Russell, C. T., Paranicas, C., et al. (2009). Sources of rotational signals in Saturn's magnetosphere. *Journal of Geophysical Research*, 114(A2), A02211. <https://doi.org/10.1029/2008JA013312>
- Kivelson, M. G., Bagenal, F., Kurth, W. S., Neubauer, F. M., Paranicas, C., & Saur, J. (2004). Magnetospheric interactions with satellites. In F. Bagenal, T. E. Dowling, & W. B. McKinnon (Eds.), *Jupiter: The planet, satellites and magnetosphere* (pp. 513–536). Cambridge University Press.
- Kivelson, M. G., Khurana, K. K., Russell, C. T., Volwerk, M., Walker, R. J., & Zimmer, C. (2000). Galileo magnetometer measurements: A stronger case for a subsurface ocean at Europa. *Science*, 289(5483), 1340–1343. <https://doi.org/10.1126/science.289.5483.1340>
- Kivelson, M. G., Khurana, K. K., Stevenson, D. J., Bennett, L., Joy, S., Russell, C. T., et al. (1999). Europa and Callisto: Induced or intrinsic fields in a periodically varying plasma environment. *Journal of Geophysical Research*, 104(A3), 4609–4626. <https://doi.org/10.1029/1998JA900095>
- Kivelson, M. G., Khurana, K. K., & Volwerk, M. (2009). Europa's interaction with the Jovian magnetosphere. In R. T. Pappalardo, W. B. McKinnon, & K. K. Khurana (Eds.), *Europa* (p. 545). University of Arizona Press, The University of Arizona Space Science Series.
- Kliore, A. J., Anabtawi, A., Herrera, R. G., Asmar, S. W., Nagy, A. F., Hinson, D. P., & Flasar, F. M. (2002). Ionosphere of Callisto from Galileo radio occultation observations. *Journal of Geophysical Research*, 107(A11), SIA19-1–SIA19-7. <https://doi.org/10.1029/2002JA009365>
- Kollmann, P., Hill, M. E., McNutt, R. L., Brown, L. E., Allen, R. C., Clark, G., et al. (2019). Suprathermal ions in the outer heliosphere. *The Astrophysical Journal*, 876(1), 46. <https://doi.org/10.3847/1538-4357/ab125f>
- Krimigis, S. M., Mitchell, D. G., Hamilton, D. C., Livi, S., Dandouras, J., Jaskulek, S., et al. (2004). Magnetosphere imaging instrument (MIMI) on the Cassini mission to Saturn/Titan. *Space Science Reviews*, 114(1–4), 233–329. <https://doi.org/10.1007/s11214-004-1410-8>
- Liang, M.-C., Lane, B. F., Pappalardo, R. T., Allen, M., & Yung, Y. L. (2005). Atmosphere of Callisto. *Journal of Geophysical Research*, 110(E2). <https://doi.org/10.1029/2004JE002322>
- Lindsay, B. G., & Stebbings, R. F. (2005). Charge transfer cross sections for energetic neutral atom data analysis. *Journal of Geophysical Research*, 110(A12), A12213. <https://doi.org/10.1029/2005JA011298>
- Lindsay, B. G., Yu, W. S., & Stebbings, R. F. (2005). Cross sections for charge-changing processes involving kilo-electron-volt H and H<sup>+</sup> with CO and CO<sub>2</sub>. *Physical Review A*, 71(3), 032705. <https://doi.org/10.1103/PhysRevA.71.032705>
- Liuzzo, L., Feyerabend, M., Simon, S., & Motschmann, U. (2015). The impact of Callisto's atmosphere on its plasma interaction with the Jovian magnetosphere. *Journal of Geophysical Research: Space Physics*, 120(11), 9401–9427. <https://doi.org/10.1002/2015JA021792>
- Liuzzo, L., Poppe, A. R., Addison, P., Simon, S., Nénon, Q., & Paranicas, C. (2022). Energetic magnetospheric particle fluxes onto Callisto's atmosphere. *Journal of Geophysical Research: Space Physics*, 127(11), e2022JA030915. <https://doi.org/10.1029/2022JA030915>
- Liuzzo, L., Poppe, A. R., Nénon, Q., Simon, S., & Addison, P. (2024). Constraining the influence of Callisto's perturbed electromagnetic environment on energetic particle observations. *Journal of Geophysical Research: Space Physics*, 129(2), e2023JA032189. <https://doi.org/10.1029/2023JA032189>
- Liuzzo, L., Simon, S., & Feyerabend, M. (2018). Observability of Callisto's inductive signature during the JUpiter ICY moons explorer mission. *Journal of Geophysical Research: Space Physics*, 123(11), 9045–9054. <https://doi.org/10.1029/2018JA025951>
- Liuzzo, L., Simon, S., Feyerabend, M., & Motschmann, U. (2016). Disentangling plasma interaction and induction signatures at Callisto: The Galileo C10 flyby. *Journal of Geophysical Research: Space Physics*, 121(9), 8677–8694. <https://doi.org/10.1002/2016JA023236>
- Liuzzo, L., Simon, S., Feyerabend, M., & Motschmann, U. (2017). Magnetic signatures of plasma interaction and induction at Callisto: The Galileo C21, C22, C23, and C30 flybys. *Journal of Geophysical Research: Space Physics*, 122(7), 7364–7386. <https://doi.org/10.1002/2017JA024303>
- Liuzzo, L., Simon, S., & Regoli, L. (2019a). Energetic electron dynamics near Callisto. *Planetary and Space Science*, 179, 104726. <https://doi.org/10.1016/j.pss.2019.104726>

- Liuzzo, L., Simon, S., & Regoli, L. (2019b). Energetic ion dynamics near Callisto. *Planetary and Space Science*, 166, 23–53. <https://doi.org/10.1016/j.pss.2018.07.014>
- Mauk, B. H., Allegri, F., Bagenal, F., Bolton, S. J., Clark, G., Connerney, J. E. P., et al. (2020). Energetic neutral atoms from Jupiter's polar regions. *Journal of Geophysical Research: Space Physics*, 125(12), e2020JA028697. <https://doi.org/10.1029/2020JA028697>
- Mauk, B. H., Clark, G., Allegri, F., Bagenal, F., Bolton, S. J., Connerney, J. E. P., et al. (2020). Juno energetic neutral atom (ENA) remote measurements of magnetospheric injection dynamics in Jupiter's Io torus regions. *Journal of Geophysical Research: Space Physics*, 125(5), e2020JA027964. <https://doi.org/10.1029/2020JA027964>
- Mauk, B. H., Mitchell, D., Krimigis, S., Roelof, E., & Paranicas, C. (2003). Energetic neutral atoms from a trans-Europa gas torus at Jupiter. *Nature*, 421(6926), 920–922. <https://doi.org/10.1038/nature01431>
- Mauk, B. H., Mitchell, D., McEntire, R., Paranicas, C., Roelof, E., Williams, D., et al. (2004). Energetic ion characteristics and neutral gas interactions in Jupiter's magnetosphere. *Journal of Geophysical Research*, 109(A9), A09S12. <https://doi.org/10.1029/2003JA010270>
- Mitchell, D. G., Brandt, P. C., Roelof, E. C., Dandouras, J., Krimigis, S. M., & Mauk, B. H. (2005). Energetic neutral atom emissions from Titan interaction with Saturn's magnetosphere. *Science*, 308(5724), 989–992. <https://doi.org/10.1126/science.1109805>
- Mitchell, D. G., Brandt, P. C., Westlake, J. H., Jaskulek, S. E., Andrews, G. B., & Nelson, K. S. (2016). Energetic particle imaging: The evolution of techniques in imaging high-energy neutral atom emissions. *Journal of Geophysical Research: Space Physics*, 121(9), 8804–8820. <https://doi.org/10.1002/2016JA022586>
- Mitchell, D. G., Cheng, A. F., Krimigis, S. M., Keath, E. P., Jaskulek, S. E., Mauk, B. H., & Drake, V. A. (1993). INCA: The ion neutral camera for energetic neutral atom imaging of the Saturnian magnetosphere. *Optical Engineering*, 32(12), 3096–3101. <https://doi.org/10.1117/12.155609>
- Mitchell, D. G., Krimigis, S. M., Cheng, A. F., Hsieh, S.-L., Jaskulek, S. E., Keath, E. P., et al. (1996). Imaging-neutral camera (INCA) for the NASA Cassini mission to Saturn and Titan. *Proceedings of SPIE*, 2803, 154–161. <https://doi.org/10.1117/12.253415>
- Moirano, A., Mura, A., Hue, V., Bonfond, B., Head, L. A., Connerney, J. E. P., et al. (2024). The infrared auroral footprint tracks of Io, Europa and Ganymede at Jupiter observed by Juno-JIRAM. *Journal of Geophysical Research: Planets*, 129(3), e2023JE008130. <https://doi.org/10.1029/2023JE008130>
- Müller, J., Simon, S., Motschmann, U., Schüle, J., Glassmeier, K.-H., & Pringle, G. J. (2011). AIKEF: Adaptive hybrid model for space plasma simulations. *Computer Physics Communications*, 182(4), 946–966. <https://doi.org/10.1016/j.cpc.2010.12.033>
- Neubauer, F. M. (1980). Nonlinear standing Alfvén wave current system at Io—Theory. *Journal of Geophysical Research*, 85(A3), 1171–1178. <https://doi.org/10.1029/JA085iA03p01171>
- Neubauer, F. M. (1998). The sub-Alfvénic interaction of the Galilean satellites with the Jovian magnetosphere. *Journal of Geophysical Research*, 103(E9), 19843–19866. <https://doi.org/10.1029/97JE03370>
- Neubauer, F. M. (1999). Alfvén wings and electromagnetic induction in the interiors: Europa and Callisto. *Journal of Geophysical Research*, 104(A12), 28671–28684. <https://doi.org/10.1029/1999JA000217>
- Nordheim, T. A., Regoli, L. H., Harris, C. D. K., Paranicas, C., Hand, K. P., & Jia, X. (2022). Magnetospheric ion bombardment of Europa's surface. *The Planetary Science Journal*, 3(1), 5. <https://doi.org/10.3847/PSJ/ac382a>
- Oza, A. V., Leblanc, F., Johnson, R. E., Schmidt, C., Leclercq, L., Cassidy, T. A., & Chaufray, J.-Y. (2019). Dusk over dawn O<sub>2</sub> asymmetry in Europa's near-surface atmosphere. *Planetary and Space Science*, 167, 23–32. <https://doi.org/10.1016/j.pss.2019.01.006>
- Paranicas, C., Cooper, J. F., Garrett, H. B., Johnson, R. E., & Sturner, S. J. (2009). Europa's radiation environment and its effects on the surface. In R. T. Pappalardo, W. B. McKinnon, & K. K. Khurana (Eds.), *Europa* (p. 529). University of Arizona Press, The University of Arizona Space Science Series.
- Paranicas, C., McEntire, R. W., Cheng, A. F., Lagg, A., & Williams, D. J. (2000). Energetic charged particles near Europa. *Journal of Geophysical Research*, 105(A7), 16005–16016. <https://doi.org/10.1029/1999JA000350>
- Paranicas, C., Ratliff, J. M., Mauk, B. H., Cohen, C., & Johnson, R. E. (2002). The ion environment near Europa and its role in surface energetics. *Geophysical Research Letters*, 29(5), 18-1–18-4. <https://doi.org/10.1029/2001GL014127>
- Phipps, P., & Bagenal, F. (2021). Centrifugal equator in Jupiter's plasma sheet. *Journal of Geophysical Research: Space Physics*, 126(1), e2020JA028713. <https://doi.org/10.1029/2020JA028713>
- Plainaki, C., Cassidy, T. A., Shematovich, V. I., Milillo, A., Wurz, P., Vorburger, A., et al. (2018). Towards a global unified model of Europa's tenuous atmosphere. *Space Science Reviews*, 214(1), 40. <https://doi.org/10.1007/s11214-018-0469-6>
- Pontoni, A., Shimoyama, M., Futaana, Y., Fatemi, S., Poppe, A. R., Wieser, M., & Barabash, S. (2022). Simulations of energetic neutral atom sputtering from Ganymede in preparation for the JUICE mission. *Journal of Geophysical Research: Space Physics*, 127(1), e2021JA029439. <https://doi.org/10.1029/2021JA029439>
- Roth, L. (2021). A stable H<sub>2</sub>O atmosphere on Europa's trailing hemisphere from HST images. *Geophysical Research Letters*, 48(20), e2021GL094289. <https://doi.org/10.1029/2021GL094289>
- Roth, L., Retherford, K. D., Ivchenko, N., Schlatter, N., Strobel, D. F., Becker, T. M., & Grava, C. (2017). Detection of a hydrogen corona in HST Ly images of Europa in transit of Jupiter. *The Astronomical Journal*, 153(2), 67. <https://doi.org/10.3847/1538-3881/153/2/67>
- Roth, L., Retherford, K. D., Saur, J., Strobel, D. F., Feldman, P. D., McGrath, M. A., & Nimmo, F. (2014). Orbital apocenter is not a sufficient condition for HST/STIS detection of Europa's water vapor aurora. *Proceedings of the National Academy of Science of the United States of America*, 111(48), E5123–E5132. <https://doi.org/10.1073/pnas.1416671111>
- Roth, L., Saur, J., Retherford, K. D., Strobel, D. F., Feldman, P. D., McGrath, M. A., et al. (2016). Europa's far ultraviolet oxygen aurora from a comprehensive set of HST observations. *Journal of Geophysical Research: Space Physics*, 121(3), 2143–2170. <https://doi.org/10.1002/2015JA022073>
- Sarkango, Y., Szalay, J. R., Poppe, A. R., Nénon, Q., Kollmann, P., Clark, G., & McComas, D. J. (2023). Proton equatorial pitch angle distributions in Jupiter's inner magnetosphere. *Geophysical Research Letters*, 50(11), e2023GL104374. <https://doi.org/10.1029/2023GL104374>
- Saur, J., Strobel, D. F., & Neubauer, F. M. (1998). Interaction of the Jovian magnetosphere with Europa: Constraints on the neutral atmosphere. *Journal of Geophysical Research*, 103(E9), 19947–19962. <https://doi.org/10.1029/97JE03556>
- Schilling, N., Neubauer, F. M., & Saur, J. (2007). Time-varying interaction of Europa with the Jovian magnetosphere: Constraints on the conductivity of Europa's subsurface ocean. *Icarus*, 192(1), 41–55. <https://doi.org/10.1016/j.icarus.2007.06.024>
- Seufert, M., Saur, J., & Neubauer, F. M. (2011). Multi-frequency electromagnetic sounding of the Galilean moons. *Icarus*, 214(2), 477–494. <https://doi.org/10.1016/j.icarus.2011.03.017>
- Shen, X.-C., Li, W., Ma, Q., Nishimura, Y., Daly, A., Kollmann, P., et al. (2022). Energetic proton distributions in the inner and middle magnetosphere of Jupiter using Juno observations. *Geophysical Research Letters*, 49(16), e2022GL099832. <https://doi.org/10.1029/2022GL099832>
- Smith, H., Mitchell, D. G., Johnson, R. E., Mauk, B. H., & Smith, J. E. (2019). Europa neutral torus confirmation and characterization based on observations and modeling. *The Astrophysical Journal*, 871(1), 69. <https://doi.org/10.3847/1538-4357/aaed38>

- Spencer, J. R., Tamppari, L. K., Martin, T. Z., & Travis, L. D. (1999). Temperatures on Europa from Galileo photopolarimeter-radiometer: Nighttime thermal anomalies. *Science*, 284(5419), 1514–1516. <https://doi.org/10.1126/science.284.5419.1514>
- Szabo, P. S., Poppe, A. R., Mutzke, A., Liuzzo, L., & Mogan, S. R. C. (2024). Backscattering of ions impacting Ganymede's surface as a source for energetic neutral atoms. *The Astrophysical Journal Letters*, 963(1), L32. <https://doi.org/10.3847/2041-8213/ad2701>
- Tippens, T., Liuzzo, L., & Simon, S. (2022). Influence of Titan's variable electromagnetic environment on the global distribution of energetic neutral atoms. *Journal of Geophysical Research: Space Physics*, 127(10), e2022JA030722. <https://doi.org/10.1029/2022JA030722>
- Tippens, T., Roussos, E., Simon, S., & Liuzzo, L. (2024). A novel backtracing model to study the emission of energetic neutral atoms at Titan. *Journal of Geophysical Research: Space Physics*, 129(1), e2023JA032083. <https://doi.org/10.1029/2023JA032083>
- Tosi, F., Roatsch, T., Galli, A., Hauber, E., Lucchetti, A., Molneux, P., et al. (2024). Characterization of the surfaces and near-surface atmospheres of Ganymede, Europa and Callisto by JUICE. *Space Science Reviews*, 220(5), 59. <https://doi.org/10.1007/s11214-024-01089-8>
- Vance, S. D., Panning, M. P., Stähler, S., Cammarano, F., Bills, B. G., Tobie, G., et al. (2018). Geophysical investigations of habitability in ice-covered ocean worlds. *Journal of Geophysical Research: Planets*, 123(1), 180–205. <https://doi.org/10.1002/2017JE005341>
- Vance, S. D., Styczinski, M. J., Bills, B. G., Cochrane, C. J., Soderlund, K. M., Gómez-Pérez, N., & Paty, C. (2021). Magnetic induction responses of Jupiter's ocean moons including effects from adiabatic convection. *Journal of Geophysical Research: Planets*, 126(2), e2020JE006418. <https://doi.org/10.1029/2020JE006418>
- Vorburger, A., & Wurz, P. (2018). Europa's ice-related atmosphere: The sputter contribution. *Icarus*, 311, 135–145. <https://doi.org/10.1016/j.icarus.2018.03.022>
- Wulms, V., Saur, J., Strobel, D. F., Simon, S., & Mitchell, D. G. (2010). Energetic neutral atoms from Titan: Particle simulations in draped magnetic and electric fields. *Journal of Geophysical Research*, 115(A6), A06310. <https://doi.org/10.1029/2009JA014893>
- Zimmer, C., Khurana, K. K., & Kivelson, M. G. (2000). Subsurface Oceans on Europa and Callisto: Constraints from Galileo magnetometer observations. *Icarus*, 147(2), 329–347. <https://doi.org/10.1006/icar.2000.6456>